Review on the numerical modeling of fracture in active materials for lithium ion batteries

Journal of Power Sources 566 (2023) 232875

Contents lists available at ScienceDirect

Journal of Power Sources

journal homepage: www.elsevier.com/locate/jpowsour

Review article

Review on the numerical modeling of fracture in active materials for lithium ion batteries

Francesca Pistorio *, Davide Clerici, Francesco Mocera, Aurelio Somà

Department of Mechanical and Aerospace Engineering, Politecnico di Torino, Corso Duca degli Abruzzi, 24, 10129, Torino, Piemonte, Italy

HIGHLIGHTS

- Stress computation in active material and coupling with transport equations.
- Fundamentals of fracture mechanics models: LEFM, phase-field model and cohesive zone model.
- How to implement fracture mechanics models when dealing with LIBs.
- Literature results: fracture maps, stability conditions, crack path and fatigue.
- Relation between capacity fade and fracture mechanics.

ARTICLE INFO

Keywords:
Lithium ion battery
Fracture mechanics modeling
Multi-physics modeling
Battery damage
Mechanics of electrode materials

ABSTRACT

Lithium ion batteries are one of the most widespread energy storage systems, but they still suffer some weak points, such as safety, limited energy density, and cycle life. The latter is caused by electrochemical and mechanical damaging mechanisms. The mechanical damaging mechanisms and their interplay with electrochemistry are reviewed in this paper. Lithium ions are inserted and extracted in the active materials of electrodes during battery operation, causing the deformation of the electrode microstructure. The deformation causes stresses and fractures ultimately, inducing electrochemical reactions on the crack surfaces, which lead to performance decay, such as loss of capacity and power. Then, proper mechanical models are needed to evaluate stress and crack propagation during battery operation. This review aims to give a comprehensive explanation of the following subjects: (a) The most general electrochemical–mechanical and transport models for intercalation materials; (b) Fundamentals of fracture mechanics; (c) Numerical implementation of fracture mechanics models applied to lithium ion batteries, covering the different approaches used in literature to estimate fracture in static and dynamic conditions; (d) Summary of the results of fracture mechanics models for lithium ion batteries; (e) Degradation models based on fracture mechanics.

1. Introduction

Lithium ion batteries (LIBs) are a key element of the energy transition of these years. Their applications are extremely wide, ranging from micro and portable electronics to electric vehicles and stationary applications. The success of these energy storage systems is due to their high energy and power density, being rechargeable for many cycles, and their moderate safety and recyclability. Nevertheless, different damaging mechanisms occur in LIBs, depending on the active material of the electrode, which ultimately leads to performance decay during cycle life [1,2]. Among these, mechanical degradation is one of the most significant and widespread damaging mechanisms affecting most of the intercalation and alloy materials used in LIBs electrodes. For this reason, the research community is committed to studying these phenomena in order to find solutions to increase the life cycle of LIBs.

The elementary cell of a LIB is made of a couple of electrodes separated by a polymeric membrane. The electrodes are thin sheets deposited on a metallic foil (copper for the anode and aluminum for the cathode) that collects the electrons. Electrodes are a composite material, obtained by mixing active material particles (in the range of micrometers), conductive agents (such as carbon black, especially for graphitic electrodes), and binder (PVDF). This mixture, referred to as slurry, is smeared on the current collector, dried, and pressed to reduce the porosity. The liquid electrolyte, usually a mixture of a lithium salt ($LiPF_6$) and organic solvent (EC, DMC), fills the porosity of the electrode when the LIB is assembled.

During operation, electrochemical reactions involving the intercalation and deintercalation of lithium ions in the active material particles

* Corresponding author.
E-mail address: francesca.pistorio@polito.it (F. Pistorio).

https://doi.org/10.1016/j.jpowsour.2023.232875
Received 21 December 2022; Received in revised form 8 February 2023; Accepted 21 February 2023
Available online 16 March 2023

Nomenclature

Symbols

$\bar{D}$	Concentration dependent diffusive coefficient
$\boldsymbol{B}$	Derivative matrix of shape function
$\boldsymbol{C}$	Damping matrix
$\boldsymbol{K}$	Stiffness matrix
$\boldsymbol{Q}$	Unknown vector
$\boldsymbol{R}$	Residual matrix
$\boldsymbol{S}$	Iteration matrix
$\hat{a}$	Enriched nodal displacement
$\hat{c}$	Nodal concentration
$\hat{d}$	Nodal PF variable
$\hat{f}$	Enriched nodal displacement associated with the asymptotic function
$\hat{h}$	Enriched nodal displacement associated with the Heaviside function
$\hat{u}$	Nodal displacement
$\mathcal{H}$	Local history field
ρ_e	Specific density of electrode
a	Crack length
A_a	Specific surface area
A_c	Crack surface
A_e	Electrode surface
a_{sv}	Surface-to-volume ratio of active material particles
CF	Fraction of capacity loss
d	PF variable
E_a	Activation energy
E_k	Kinetic energy
F_e	Enrichment function
$f_{i,j}$	Dimensionless shape function for SIF computation
G	Energy release rate
i	Current density
i_{SEI}	Current density of SEI side reaction
k	Mechanical constant
K_{SEI}	SEI growth rate coefficient
K_{th}	Fatigue threshold limit
l_0	Length scale parameter
l_c	Crack width
L_e	Electrode thickness
L_{SEI}	SEI thickness
N_i	Generic shape functions
n_i	Normal versor
N_{LiS}	Lithium ion flux
n_{SEI}	Moles of Lithium ions consumed per SEI produced
Q_e	Specific capacity of electrode
r_c	Radial coordinate in crack reference frame
R_g	Gas constant
T_i	Cohesive traction
t_i	Traction vector components
t_N	Time for one cycle
u^h	Enriched displacement
V_{SEI}	SEI molar volume
W_{ext}	Work of external forces
x_{LiS}	Mole fraction of intercalated lithium ions
Y	Geometric factor
df	Thermodynamic driving force
A	Area
C	First parameter of Paris' law
c	Lithium ion concentration
D	Diffusive coefficient
E	Young modulus
e	electron
F	Faraday constant
g	Degradation function of PFM
J	J-integral
K	Stress intensity factor
L	Lagrangian
M	Molar mass
m	Second parameter of Paris' law
N	Number of cycles
Q	Capacity
R	Particle radius
r	Radial coordinate
S	Host site
T	Temperature
t	Time
U	Equilibrium potential
u	Displacement
w	Weight function
x	Cartesian direction
y	Cartesian direction

Acronyms

CZM	Cohesive zone model
DIS	Diffusion induced stress
EC	Ethylene carbonate
EPFM	Elastic–plastic fracture mechanics
FEM	Finite element method
GITT	Galvanostatic Intermittent Titration Technique
LAM	Loss of active material
LCO	Lithium cobalt oxide
LEFM	Linear elastic fracture mechanics
LFP	Lithium iron phosphate
Li	Lithium ion
LIB	Lithium ion battery
LLI	Loss of lithium inventory

of electrodes cause the current flow in the external circuit. Lithium ions intercalation causes the deformation of the active material microstructure: the greater the amount of lithium stored in the host material, the greater the change of lattice parameters of its crystalline structure, ultimately causing local deformation in the electrode microstructure.

Furthermore, lithium ions are much smaller than active material particles, then they diffuse within the particles during insertion/extraction, leading to an inhomogeneous concentration distribution, which causes differential strain and stress ultimately [3–9]. Some materials have a two-phase-behavior, meaning that phases with significant different lithium content coexist in the same particle. The sharp change in lithium content at the boundary between the different phases leads to high mechanical stress.

LMO	Lithium manganese oxide
NMC	Nickel manganese cobalt
OCV	Open circuit voltage
P2D	Partial two dimension
PF	Phase-field variable
PFM	Phase-field model
PVDF	Polyvinylidene fluoride
SEI	Solid electrolyte interphase
SEM	Scanning electron microscope
SIF	Stress intensity factor
TSL	Traction separation law
XFEM	Extended finite element method

Greek Symbols

α	Thermodynamic factor
χ	Crack surface density function
δ	Distance between crack surfaces in CZM
δ_f	Fracture separation
η	Standard overpotential
η_{SEI}	SEI overpotential
Γ	Path
γ	Activity coefficient
γ_s	Surface energy
Λ	Area enclosed in the path Γ
λ_L	Lamè constant
μ	Potential
μ_L	Lamè constant
ν	Poisson ratio
Ω	Partial molar value
Π	Total potential energy
Π_Γ	Fracture energy
Π_{el}	Elastic strain energy
Π_{Li}	Energy due to lithium diffusion
Ψ	Strain energy density
Ψ_{Li}	Chemical energy density
ρ	Density
ρ_c	Crack density
σ	Stress
σ_s	Electronic conductivity
σ_{co}	Cohesive strength
τ	Shear stress
θ	Polar coordinate in crack reference frame
θ_c	Crack propagation direction
ε	Deformation
ε_a	Accessible volume fraction of active material
$\widetilde{\Psi}_{el}$	Degradated elastic strain energy

Recursive subscripts

+	Positive charge
-	Negative charge
0	Initial
c	Circumferential
cr	Critical
el	Elastic
eq	Equivalent
h	Hydrostatic
Li	Lithium
LiS	Intercalated site with lithium ions
mech	Mechanical
min	Minimum
r	Radial
ref	Reference
S	Vacant site
solv	Solvent
max	Maximum

The stress in the electrode microstructure is a serious damaging mechanism, causing the propagation of cracks [10,11] which ultimately give rise to: (a) chemical processes consuming lithium ions; (b) the detachment of some portion of active material, no more able to host lithium ions. Both phenomena ultimately lead to progressive capacity fade.

The deformation of the crystal structure of electrodes has an impact on the dimensions of the entire LIBs, and can be observed during cycling by measuring its thickness change [12,13]: swelling is detected during charge, recovered with an opposite shrinkage during discharge.

Some reviews covered the interesting arguments regarding the electrochemical mechanical modeling of LIBs [5,14–16], but there are no reviews concerning fracture mechanics modeling in the microstructure of LIBs electrodes, as far as the authors know, except for a brief overview in [15]. On the other hand, a lot of research papers regarding the computation of fracture occurring in electrodes microstructure have been published, especially in the last five years. The works available in the literature followed different approaches, and sometimes it is difficult to understand the consistency between them. Furthermore, fracture mechanics applied to LIBs is a complex multiphysics problem, somewhat difficult to understand from specific research papers. Starting from these considerations, the authors wrote this review with a threefold purpose: (a) to clearly explain the theory of fracture mechanics applied to LIBs, analyzing in detail all the modeling approaches present in the literature; (b) to clarify the main results obtained in the literature; (c) to highlight lacks and possible developments for future works.

The work is organized as follows:

- Section 2. The most general electrochemical mechanical model used to compute stress in active materials (the driving force of fracture), based on non-dilute solution and able to consider two-phase materials, is detailed derived and explained.
- Section 3. The fundamentals of fracture mechanics are resumed, explaining their application to LIBs. The following models are covered: Linear elastic fracture mechanics (LEFM), Phase-field model (PFM) based on LEFM and Cohesive zone model (CZM).
- Section 4. The numerical implementation of the models covered in Section 3 with FEM, XFEM and cohesive elements.
- Section 5. The most significant results obtained in the literature are resumed. The results are divided on the basis of static and cyclic load. In the former case, fracture maps, crack stability, and crack path are explained.
- Section 6. The link between electrochemistry and mechanics is addressed, showing models aiming to estimate performance decay due to fracture and mechanical damage.

2. Mechanics in LIBs

The inhomogeneous lithium concentration in the active material particles caused by the diffusion of lithium ions and by the coexistence of phases with different lithium content causes differential strains, leading to the so-called diffusion induced stress (DIS) [3–9], as sketched in Fig. 1a.

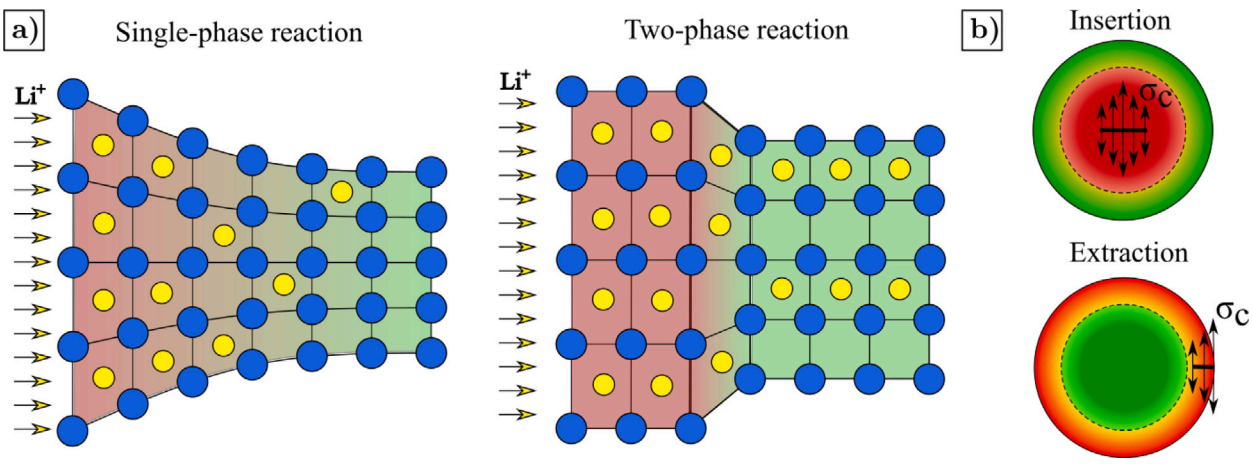

Fig. 1. (a) Mechanical stress resulting from inhomogeneous concentration due to lithium diffusion and phase transition. (b) Mode I fracture caused by the hoop stress σ_c induced by lithium insertion and extraction.

Hoop stress in the particle is the driving force for crack propagation according to mode I. Hoop stress is tensile in the core during insertion, viceversa it is tensile on the surface during extraction, then cracks in different locations propagate during lithiation or delithiation, according to Fig. 1b.

Active material particles are quasi-spherical according to scanning electrode microscope (SEM) observations [17], then a spherical domain is considered for sake of simplicity. Consequently, all the equations are written according to the axisymmetric hypothesis, and the radial direction is the only variable involved. Therefore, displacement, strain, stress, concentration, boundary conditions, and material properties do not change along the two hoop directions. The assumption about the axisymmetric boundary condition is compatible with most of the materials having a 3D diffusion channel, but is not suitable for those materials, such as Lithium Iron Phosphate (LFP), presenting a 1D diffusion channel and, thus, non-axisymmetric boundary conditions [17].

DIS in electrode microstructure is a multi-physics problem, as mechanical and transport (diffusive/chemical) phenomena occur simultaneously and affect each other. Then, the physics of the two domains is explained in the next sections.

2.1. Mechanical equations

The mechanical field in a spherical particle is modeled according to the constitutive, congruence, and equilibrium equations reported in Eqs. (1)a-c [7]. This set of equations allows computing displacement, deformation, and stress caused by the concentration of intercalated lithium ions, referred to as c_{LiS}. The constitutive equations (Eq. (1)a) are composed of the elastic (first) term, and chemical (second) term, which depends on the concentration of intercalated lithium ions and links chemistry with mechanics.

Constitutive:

$$\varepsilon_r = \frac{1}{E}(\sigma_r - 2\nu\sigma_c) + \frac{\Omega c_{LiS}}{3};\ \ \varepsilon_c = \frac{1}{E}[(1-\nu)\sigma_c - \nu\sigma_r) + \frac{\Omega c_{LiS}}{3} \tag{1a}$$

Congruence:

$$\varepsilon_r = \frac{\partial u}{\partial r};\ \varepsilon_c = \frac{u}{r} \tag{1b}$$

Equilibrium:

$$\frac{\partial \sigma_r}{\partial r} + \frac{2}{r}(\sigma_r - \sigma_c) = 0 \tag{1c}$$

Where σ_r, ε_r, σ_c, ε_c are radial and circumferential stress and strain, respectively, Ω is the partial molar volume of lithium ions in the host material and u is the radial displacement. The displacement solution is got replacing the congruence equations (Eq. (1)b) in the constitutive ones (Eq. (1)a), the latter in the equilibrium Equation (Eq. (1)c), and integrating twice. Then, strains and stresses are computed from displacement solution with congruence and constitutive equations, and their results are reported in Eqs. (2)a-c [7]. An analytical expression of the solution is obtained thanks to the simple geometry, however, it is generally not possible to obtain a close solution, even for the mechanical field.

Displacement:

$$u(r) = \frac{\Omega}{3(1-\nu)}\left[(1+\nu)\frac{1}{r^2}\int_0^r c_{LiS}(r)r^2\,dr + 2(1-2\nu)\frac{r}{R^3}\int_0^R c_{LiS}(r)r^2\,dr\right] \tag{2a}$$

Radial stress:

$$\sigma_r(r) = \frac{2\Omega}{3}\frac{E}{1-\nu}\left[\frac{1}{R^3}\int_0^R c_{LiS}(r)r^2\,dr - \frac{1}{r^3}\int_0^r c_{LiS}(r)r^2\,dr\right] \tag{2b}$$

Hoop stress:

$$\sigma_c(r) = \frac{\Omega}{3}\frac{E}{1-\nu}\left[\frac{2}{R^3}\int_0^R c_{LiS}(r)r^2\,dr + \frac{1}{r^3}\int_0^r c_{LiS}(r)r^2\,dr - c_{LiS}(r)\right] \tag{2c}$$

The hydrostatic stress is computed according to Eq. (3), and it will be needed in the transport model.

$$\sigma_h = \frac{(\sigma_r + 2\sigma_c)}{3} = \frac{2\Omega E}{9(1-\nu)}\left[\frac{3}{R^3}\int_0^R c_{LiS}(r)r^2\,dr - c_{LiS}(r)\right] \tag{3}$$

At this stage, lithium concentration in intercalated sites c_{LiS} is needed to compute displacement, strain, and stress.

2.2. Transport equations

The most general approach to describe lithium transport and intercalation is using a binary solution model, resulting in a concentration-dependent diffusion coefficient. This approach is based on the work of Newman et al. [3,6], later developed by Farkhondeh et al. [18] and Baker et al. [19]. Other authors [20–22] followed a similar approach, but their derivation appears less rigorous and is not considered in this review.

The dependence of the diffusion coefficient on the mole fraction of lithium is twofold. Firstly, it models the coupling between mechanical and transport equations, indeed the diffusion of lithium ions is the cause of mechanical stresses, and stress affects diffusion at the same time. Secondly, it models the phase transition occurring in some materials on the basis of the open circuit voltage (OCV), according to the non-ideal solution theory.

At first, the most general model is explained in Section 2.2.1, considering a non-ideal (or concentrated) solution, as well as the coupling between transport and mechanical equations. Then, the dilute approach is considered in Section 2.2.2, neglecting the dependence of the diffusion coefficient on the OCV, but still considering the coupling between mechanical and transport equations. Finally, the uncoupled model is covered in Section 2.2.3, where the coupling between mechanical and transport equations is neglected, and the diffusion coefficient is no longer dependent on lithium concentration.

2.2.1. Non-ideal solution model

The binary solution consists of unoccupied sites (S) and li-intercalated sites (LiS) in the host material, according to the following reaction:

$$Li^{+}_{electrolyte} + e^{-}_{matrix} + S_{host} \rightleftharpoons LiS_{host} \tag{4}$$

The mass conservation law (Eq. (5)) tells how the concentration of intercalated lithium ions (c_{LiS}) changes in time inside the particle, as a result of the molar flux which causes the ions kinetic (N_{LiS}). The particle is assumed to be a sphere, then Eq. (5) is written in radial coordinates (r) exploiting the spherical symmetry.

$$\frac{\partial c_{LiS}}{\partial t} + \frac{1}{r^2}\frac{\partial}{\partial r}(r^2 N_{LiS}) = 0 \tag{5}$$

The diffusion of lithium ions within the particle is driven by the thermodynamic potential (μ) which has two contributions: chemical (μ_{LiS}) and mechanical (μ_{mech}), as expressed in Eq. (6)a. Temperature is assumed constant within the particle, so it is neglected as a source of diffusion. Then, lithium ions are driven by the gradient of the thermodynamic potential according to the driving force (df_{LiS}) expressed in Eq. (6)b [6].

$$\mu = \mu_{LiS} + \mu_{mech} = \left(\mu^0_{LiS} + R_g T \ln(\gamma_{LiS} x_{LiS})\right) + \left(-\Omega\sigma_h\right) \tag{6a}$$

$$df_{LiS} = c_{LiS}\left(\nabla\mu_{LiS} - \Omega\nabla\sigma_h\right) \tag{6b}$$

Where μ^0_{LiS} is chemical potential at the reference state, R_g is the gas constant, T is the temperature, x_{LiS} is the mole fraction of intercalated lithium ions and γ_{LiS} is the activity coefficient which takes into account the non-ideality of the solution. As a consequence, lithium ions are driven to areas with a lower concentration and tensile (positive sign), or less compressive stress.

The molar flux (N_{LiS}) is defined in Eq. (7) according to Eq. (6), assuming that the flux of vacant and occupied species sums to zero, meaning that the saturation concentration of lithium ions in the host (c_{max}) remains constant [19].

$$\begin{aligned} N_{LiS} &= -\frac{D}{R_g T} df_{LiS} = \\ &= -\frac{D}{R_g T} c_{LiS}\left[\nabla\mu_{LiS} - \Omega\nabla\sigma_h\right] = \\ &= -\frac{D}{R_g T} c_{LiS}\left[\frac{\partial\mu_{LiS}}{\partial x_{LiS}} - \Omega\frac{\partial\sigma_h}{\partial x_{LiS}}\right]\nabla x_{LiS} \end{aligned} \tag{7}$$

Where D is the diffusion coefficient of lithium in the host material.

It is useful to differentiate the gradient of chemical potential and hydrostatic stress in Eq. (7), since both depend on lithium concentration, which depends on the radial coordinate in turn. Then, an explicit expression of $\frac{\partial\mu_{LiS}}{\partial x_{LiS}}$ and $\frac{\partial\sigma_h}{\partial x_{LiS}}$ will be obtained to solve the mass conservation problem.

Chemical potential. At first, the term $\frac{\partial\mu_{LiS}}{\partial x_{LiS}}$ is considered. The chemical potential of the species LiS (μ_{LiS}) is written according to Eq. (8).

$$\mu_{LiS} = \mu^0_{LiS} + R_g T \ln(\gamma_{LiS} x_{LiS}) \tag{8}$$

The differential of the chemical potential of the species LiS with respect to the mole fraction x_{LiS} is computed in Eq. (9), differentiating Eq. (8).

$$\begin{aligned} \frac{\partial\mu_{LiS}}{\partial x_{LiS}} = \frac{\partial}{\partial x_{LiS}}\left[R_g T ln(\gamma_{LiS} x_{LiS})\right] &= R_g T \frac{\partial}{\partial x_{LiS}}\left[ln(\gamma_{LiS}) + \ln(x_{LiS})\right] = \\ &= \frac{R_g T}{x_{LiS}}\left[\frac{\partial \ln(\gamma_{LiS})}{\partial \ln(x_{LiS})} + 1\right] = \\ &= \frac{R_g T}{x_{LiS}}\alpha \end{aligned} \tag{9}$$

The term $\alpha = \left[\frac{\partial \ln(\gamma_{LiS})}{\partial \ln(x_{LiS})} + 1\right]$ is the so-called thermodynamic factor, and it takes into account the non-ideality of the solution.

The expression of the thermodynamic factor in Eq. (9) is written in an unsuitable form to be computed experimentally. Then, a relation between the thermodynamic factor and equilibrium potential is pursued.

The equilibrium potential U of active material with respect to Li^+, even referred to as open circuit voltage (OCV) is expressed in Eq. (10).

$$FU = \mu^0_{Li} + \mu_S - \mu_{LiS} \tag{10}$$

Where F is the Faraday constant, μ^0_{Li}, μ_S and μ_{Lis} are the chemical potential of pure lithium metal, empty and li-intercalated sites in the host material, respectively.

Then, Eq. (10) is differentiated with respect to x_{LiS}, according to Eq. (11).

$$F\frac{\partial U}{\partial x_{LiS}} = \frac{\partial\mu_S}{\partial x_{LiS}} - \frac{\partial\mu_{LiS}}{\partial x_{LiS}} \tag{11}$$

Then, the differentiation of the chemical potential of the empty sites with respect to the mole fraction of lithium ($\frac{\partial\mu_S}{\partial x_{LiS}}$) is obtained isolating μ_S from the Gibbs–Duhem equation ($x_{LiS} d\mu_{LiS} + x_S d\mu_S = 0$) and deriving with respect to x_{LiS}, according to Eq. (12).

$$\frac{\partial\mu_S}{\partial x_{LiS}} = -\frac{\partial\mu_{LiS}}{\partial x_{LiS}}\frac{x_{LiS}}{x_S} \tag{12}$$

The differentiation of the chemical potential of the li-intercalated sites with respect to the mole fraction of lithium ($\frac{\partial\mu_{LiS}}{\partial x_{LiS}}$) is got in Eq. (13) replacing Eq. (12) in Eq. (11), and considering that the mole fractions of vacant and occupied sites sum to one ($x_{LiS} + x_S = 1$)

$$\frac{\partial\mu_{LiS}}{\partial x_{LiS}} = -F(1 - x_{LiS})\frac{\partial U(x_{LiS})}{\partial x_{LiS}} \tag{13}$$

Finally, the expression of thermodynamic factor is got in Eq. (14), equating $\frac{\partial\mu_{LiS}}{\partial x_{LiS}}$ reported in Eq. (9) with Eq. (13).

$$\alpha(x_{LiS}) = 1 + \frac{\partial \ln(\gamma_{LiS})}{\partial \ln(x_{LiS})} = -\frac{F}{R_g T} x_{LiS}(1 - x_{LiS})\frac{\partial U(x_{LiS})}{\partial x_{LiS}} \tag{14}$$

The expression in Eq. (14) allows practically computing the thermodynamic factor from OCV measurements. It is observed that the OCV curve is flat where the two-phase reaction occurs, making its derivative almost zero, and eventually decreasing the thermodynamic factor and, then, the chemical driving force (Eq. (9)). It will be explained in the "final equations" paragraph that the chemical driving force is proportional to the overall diffusion coefficient, then diffusion decreases as well. The localized decrease of diffusion coefficient causes a sharp variation of lithium concentration, which mimic pretty well the concentration difference between the coexistent phases.

OCV depends just on lithium concentration, then even its derivative $\frac{\partial U}{\partial x_{LiS}}$ is a function of lithium concentration. For this reason,

the thermodynamic factor makes the diffusion coefficient dependent on lithium content. Interestingly, Baker et al. [19] showed that the measurements of diffusion coefficient with Galvanostatic Intermittent Titration Technique (GITT) fit pretty well with composition-dependent diffusion coefficient computed with concentrated theory.

Mechanical potential. The term $\frac{\partial \sigma_h}{\partial x_{LiS}}$ is computed deriving the hydrostatic stress reported early in Eq. (2).

$$\frac{\partial \sigma_h}{\partial x_{LiS}} = -\frac{2\Omega E}{9(1-\nu)} \tag{15}$$

Final equations. The lithium molar flux (N_{LiS}) reported in Eq. (7) is rewritten in Eq. (16)a-b, according to the results of Eqs. (9), (14) and (15).

$$N_{LiS} = -Dc_{max}\left[-\frac{F}{RT}x_{LiS}(1-x_{LiS})\frac{\partial U(x_{LiS})}{\partial x_{LiS}} + x_{LiS}\frac{2\Omega^2 Ec_{max}}{9(1-\nu)RT}\right]\frac{\partial x_{LiS}}{\partial r} \tag{16a}$$

$$N_{LiS} = -Dc_{max}\left[\alpha + x_{LiS}k\right]\frac{\partial x_{LiS}}{\partial r} \tag{16b}$$

Where the saturation concentration $c_{max} = c_{LiS}/x_{LiS}$ and $k = \frac{2\Omega^2 Ec_{max}}{9(1-\nu)RT}$.

Eq. (16)a-b can be rewritten as the Fick's law (Eq. (17)a) defining the concentration-dependent diffusion coefficient ($\bar{D}(x_{LiS})$) reported in Eq. (17)b.

$$N_{LiS} = -\bar{D}(x_{LiS})c_{max}\frac{\partial x_{LiS}}{\partial r} \tag{17a}$$

$$\bar{D}(x_{LiS}) = D\left[-\frac{F}{RT}x_{LiS}(1-x_{LiS})\frac{\partial U(x_{LiS})}{\partial x_{LiS}} + x_{LiS}\frac{2\Omega^2 Ec_{max}}{9(1-\nu)RT}\right] = D\left[\alpha + x_{LiS}k\right] \tag{17b}$$

Finally, the lithium molar flux in Eq. (16) is replaced in the mass conservation (Eq. (5)) to obtain the first of Eq. (18). Then, the distribution of lithium ions concentration in the spherical particle is obtained solving the problem described by Eq. (18), where $N_{surface}(t)$ is the lithium ions flux applied on the external surface, which is generally time-dependent.

$$\begin{cases} \frac{\partial c}{\partial t} = Dc_{max}\left[\frac{2}{r}\left(\alpha + x_{LiS}k\right)\frac{\partial x_{LiS}}{\partial r} + \left(\frac{\partial \alpha}{\partial x_{LiS}} + k\right)\left(\frac{\partial x_{LiS}}{\partial r}\right)^2 + \left(\alpha + x_{LiS}k\right)\frac{\partial^2 x_{LiS}}{\partial r^2}\right] \\ \left.\frac{\partial c(r,t)}{\partial r}\right|_{r=R} = N_{surface}(t), \qquad \text{for} \quad t \geq 0 \\ \left.\frac{\partial c(r,t)}{\partial r}\right|_{r=0} = 0, \qquad \text{for} \quad t \geq 0 \end{cases} \tag{18}$$

The lithium flux over the particle surface is assumed to be known from the results of an electrochemical model, e.g. single particle model (SPM) or partial 2D model (P2D) [23].

The solution to the problem in Eq. (18) cannot be computed analytically. Finite difference (FDM) [6,18,19] of finite element models (FEM) are usually employed, especially implemented in COMSOL Multiphysics [20,24].

2.2.2. Ideal solution model

The ideal or dilute solution model does not consider the interaction between lithium ions, then the activity coefficient γ_{LiS} is equal to 1, thus the model neglects the correction on concentration through γ_{LiS} in Eq. (8). Consequently, the thermodynamic factor α is equal to 1, and the concentration-dependent diffusion coefficient ($\bar{D}(x_{LiS})$), reported previously in Eq. (17)b, modifies according to Eq. (19)b.

$$N_{LiS} = -\bar{D}(x_{LiS})c_{max}\frac{\partial x_{LiS}}{\partial r} \tag{19a}$$

$$\bar{D}(x_{LiS}) = D\left[1 + x_{LiS}\frac{2\Omega^2 Ec_{max}}{9(1-\nu)RT}\right] = D\left[1 + x_{LiS}k\right] \tag{19b}$$

Then, the transport equation changes as follows:

$$\begin{cases} \frac{\partial c}{\partial t} = Dc_{max}\left[\frac{2}{r}\left(1 + x_{LiS}k\right)\frac{\partial x_{LiS}}{\partial r} + k\left(\frac{\partial x_{LiS}}{\partial r}\right)^2 + \left(1 + x_{LiS}k\right)\frac{\partial^2 x_{LiS}}{\partial r^2}\right] \\ \left.\frac{\partial c(r,t)}{\partial r}\right|_{r=R} = N_{surface}(t) \qquad \text{for} \quad t \geq 0 \\ \left.\frac{\partial c(r,t)}{\partial r}\right|_{r=0} = 0 \qquad \text{for} \quad t \geq 0 \end{cases} \tag{20}$$

The analytical solution of Eq. (20) is known [7], and it exploits the solution of Fick's problem in Eq. (19)a, defining a concentration-dependent diffusion coefficient according to Eq. (19)b.

The coupling between the mechanical and transport equations is still considered in this model.

2.2.3. Uncoupled model

The simplest approach consists of neglecting both activity correction, thus possible phase transitions, and the coupling between mechanical and transport equations, defining the so-called uncoupled model [7].

In this model, the term $\Omega\nabla\sigma_h$ in the thermodynamic driving force (Eq. (6)b) is neglected, as well as the activity coefficient in the chemical potential is considered unitary, as in the model of Section 2.2.2. Considering these assumptions, $\bar{D}$=D and the lithium molar flux in Eq. (16) is rewritten according to Eq. (21).

$$N_{LiS} = -Dc_{max}\frac{\partial x_{LiS}}{\partial r} \tag{21}$$

Where D is the nominal diffusion coefficient, which is no longer concentration-dependent. Then, the transport equations are written according to Eq. (22).

$$\begin{cases} \frac{\partial c}{\partial t} = Dc_{max}\frac{\partial^2 x_{LiS}}{\partial r^2} \\ \left.\frac{\partial c(r,t)}{\partial r}\right|_{r=R} = N_{surface}(t) \quad \text{for} \quad t \geq 0 \\ \left.\frac{\partial c(r,t)}{\partial r}\right|_{r=0} = 0 \qquad \text{for} \quad t \geq 0 \end{cases} \tag{22}$$

The uncoupled model overestimates stress, because the coupling increases the diffusion coefficient, as the stress gradient is coherent with concentration gradient [7,9].

2.3. Concluding remarks

The mechanical model of an active material spherical particle subjected to lithium intercalation is explained. Lithium intercalation causes a deformation proportional to its concentration, which is added to the elastic deformation in the constitutive equations.

Lithium concentration is then computed by solving the transport equation, which can be written according to three different approaches:

- **Non-ideal solution and coupled model.** The non-ideality of the solution is considered to describe the phase-changing behavior of the material. Furthermore, the mutual influence (referred to as coupling) between the mechanical and the transport fields is considered.
- **Ideal solution and coupled model.** The non-ideality of the solution is neglected, and the activity coefficient γ_{LiS} is set to one. Just single-phase material can be described by this model. The coupling between the mechanical and the transport fields is still considered.

Table 1
Summary of the components of lithium flux written as $N_{Lis} = -\frac{c_{LiS}D}{RT}\left[\frac{\partial \mu_{LiS}}{\partial x_{LiS}} - \Omega\frac{\partial \sigma_h}{\partial x_{LiS}}\right]\nabla x_{LiS}$, resulting lithium flux, and apparent concentration-dependent diffusion coefficient, considering the traditional Fick law: $N_{LiS} = -\bar{D}\nabla x_{LiS}$.

	Non-ideal model (coupled)	Ideal model (coupled)	Ideal model (uncoupled)
$\frac{\partial \mu}{\partial x_{LiS}}$	$\frac{RT}{x_{LiS}}\alpha$	$\frac{RT}{x_{LiS}}$	$\frac{RT}{x_{LiS}}$
$\frac{\partial \sigma_h}{\partial x_{LiS}}$	$-\frac{2\Omega E}{9(1-\nu)}$	$-\frac{2\Omega E}{9(1-\nu)}$	Neglected
N_{LiS}	$-Dc_{max}\left[\alpha + x_{LiS}k\right]\frac{\partial x_{LiS}}{\partial r}$	$-Dc_{max}\left[1 + x_{LiS}k\right]\frac{\partial x_{LiS}}{\partial r}$	$-Dc_{max}\frac{\partial x_{LiS}}{\partial r}$
$\bar{D}$	$D\left[\alpha + x_{LiS}k\right]$	$D\left[1 + x_{LiS}k\right]$	D

- **Ideal solution and uncoupled model.** The non-ideality of the solution is neglected, and the activity coefficient γ_{LiS} is set to one. Just single-phase material can be described by this model. Furthermore, the coupling between the mechanical and the transport fields is neglected, and transport is no longer affected by mechanical stress.

Displacement, strain, and stress can be computed by Eq. (2) once concentration distribution is solved using the chosen model according to Eqs. (18), or (20) or (22).

For sake of clarity, the components of lithium flux, the resulting lithium flux, and the concentration-dependent diffusion coefficient are listed in Table 1 for each model.

In the following sections, the subscript "LiS" is neglected, and the concentration of lithium ions in active material will be simply referred to as "c".

The mechanical stress computed with the DIS model is the driving force of crack propagation in the active materials of electrodes, thus the DIS model constitutes the basis of fracture mechanics modeling in LIBs.

3. Fundamentals of fracture mechanics applied to LIBs

Stresses and displacements computed in Section 2 are the basis of fracture mechanics models, which aim to give a local estimation of stress and displacement at the crack tip.

LEFM theory describes fracture in linear elastic material, i.e. when the plastic zone at the crack tip is small compared to the crack length.

The main drawback of LEFM theory is that it can predict fracture only for a body with pre-existent cracks, thus it is not able to model the crack initiation stage. An alternative approach is the CZM theory, which allows solving the fracture problem even when the non-linear area near the crack tip is not negligible and without assuming pre-existent cracks.

The PFM represents an additional and effective alternative to the discontinuous approach of LEFM theory. It represents a stand-alone modeling strategy able to predict the initiation, growth, merging, branching, and arrest of cracks, in arbitrary dimensions and geometries, both in brittle and ductile materials.

In the following sections, an overview of LEFM, CZM, and PFM theories is given, with special regard to their application to predict fracture in LIBs both due to static and cyclic loading.

3.1. LEFM

The stress state at the crack tip can be characterized using a stress-based approach or an energetic-based approach. According to the LEFM theory, the stress at the crack tip is infinite, thus suitable parameters are needed to properly describe the stress state at the crack tip.

LEFM theory predicts the stress field singularity at the crack tip in terms of stress intensity factor (SIF) (K), energy release rate (G), or J-integral.

3.1.1. Stress intensity factor K

The SIF (K) is the most used parameter in LEFM to characterize the stress field at the crack tip. The magnitude of K depends on the geometry of the specimen, the size and location of the crack, and the magnitude of the applied stress, according to Eq. (23).

$$K = Y\sigma\sqrt{\pi a} \tag{23}$$

Where Y is a geometric factor accounting for the specimen geometry and crack location, σ is the applied stress, and a is the crack length. According to Irwin [25], the stress field at the crack tip can be expressed as a function of K, as reported in Eq. (24).

$$\sigma_{ij} = \frac{K}{\sqrt{2\pi r_c}} f_{ij}(\theta) \tag{24}$$

Where σ_{ij} are the components of the stress tensor, r_c and θ are the polar coordinates with origin at the crack tip as depicted in Figure S1a, and $f_{ij}(\theta)$ is a dimensionless shape function. Eq. (24) shows that a stress singularity proportional to $\frac{1}{\sqrt{r_c}}$ exists at the crack tip.

A crack subjected to any arbitrary loading can be resolved into three independent cracking modes: mode I (tensile), mode II (shearing) and mode III (tearing), as shown in Figure S1b. Consequently, three different SIFs can be used to characterize the stress field at the crack tip. The corresponding stress fields due to modes I, II and III are expressed by Eqs. (25)a, b and c, respectively.

$$\begin{cases} \sigma_{xx} = \frac{K_I}{\sqrt{2\pi r_c}}\cos(\theta/2)[1 - \sin(\theta/2)\sin(3\theta/2)] \\ \sigma_{yy} = \frac{K_I}{\sqrt{2\pi r_c}}\cos(\theta/2)[1 + \sin(\theta/2)\sin(3\theta/2)] \\ \tau_{xy} = \frac{K_I}{\sqrt{2\pi r_c}}\sin(\theta/2)\cos(\theta/2)\cos(3\theta/2) \\ \sigma_{zz} = \nu(\sigma_{xx} + \sigma_{yy}) \\ \tau_{xz} = \tau_{yz} = 0, \end{cases} \tag{25a}$$

$$\begin{cases} \sigma_{xx} = \frac{K_{II}}{\sqrt{2\pi r_c}}\sin(\theta/2)[2 + \cos(\theta/2)\cos(3\theta/2)] \\ \sigma_{yy} = \frac{K_{II}}{\sqrt{2\pi r_c}}\sin(\theta/2)\cos(\theta/2)\cos(3\theta/2) \\ \tau_{xy} = \frac{K_{II}}{\sqrt{2\pi r_c}}\cos(\theta/2)[1 - \sin(\theta/2)\sin(3\theta/2)] \\ \sigma_{zz} = \nu(\sigma_{xx} + \sigma_{yy}) \\ \tau_{xz} = \tau_{yz} = 0. \end{cases} \tag{25b}$$

$$\begin{cases} \sigma_{xx} = \sigma_{yy} = \sigma_{zz} = \tau_{yz} = 0 \\ \tau_{xz} = \frac{K_{III}}{\sqrt{2\pi r_c}} \\ \tau_{yz} = \frac{K_{III}}{\sqrt{2\pi r_c}}\cos(\theta/2). \end{cases} \tag{25c}$$

where K_i is the SIF relative to mode i.

3.1.2. Energy release rate G

The energy release rate G is defined as the decrease of the total potential energy per increase in fracture length (or surface area for 3D

problems), according to Eq. (26).

$$G = -\frac{\partial \Pi}{\partial a} \tag{26}$$

Where Π is the total potential energy and a is the crack length (or area). The total potential energy is defined in Eq. (27).

$$\Pi = \Pi_{el} + \Pi_{\Gamma} - W_{ext} \tag{27}$$

Where Π_{el} is the elastic strain energy, Π_{Γ} is the fracture energy and W_{ext} is the work done by external forces. For a given mode i, the energy release rate G_i is a function of the corresponding SIF, as expressed by Eqs. (28)a, b and c for mode I, II and III, respectively.

$$G_I = \begin{cases} \frac{1}{E} K_I^2 & \text{plane stress} \\ \frac{1-\nu^2}{E} K_I^2 & \text{plane strain} \end{cases} \tag{28a}$$

$$G_{II} = \frac{1-\nu^2}{E} K_{II}^2 \tag{28b}$$

$$G_{III} = \frac{K_{III}^2}{2\mu_L} \tag{28c}$$

Where E is the Young modulus, ν is the Poisson ratio and μ_L is the shear modulus. The energy release rate G due to the combination of all cracking modes is obtained by applying the superimposition of effects, as reported in Eq. (29).

$$G = G_I + G_{II} + G_{III} \tag{29}$$

3.1.3. J-integral

The J-integral was proposed independently by Rice [26] and Cherepanov [27] as a contour integral characterizing the crack tip state in elastic–plastic materials. The J-integral proposed by Rice for a 2D fracture problem is expressed in Eq. (30), according to Figure S2 and considering an arbitrary counterclockwise path Γ around the crack tip.

$$J = \int_{\Gamma} \left(\psi_{el} dy - t_i \frac{\partial u_i}{\partial x} \right) ds \tag{30}$$

Where $\psi_{el} = \int_0^{\varepsilon_{ij}} \sigma_{ij} d\varepsilon_{ij}$ is the strain energy density, σ_{ij} are the components of the stress tensor, ε_{ij} are the components of the strain tensor, $t_i = \sigma_{ij} n_j$ are the components of the traction vector acting on the path Γ, n_j is the versor normal to Γ, u_i are the displacement components, x and y are the coordinates parallel and perpendicular to the crack direction respectively, and ds is the element length along Γ.

Eq. (30) states that the total energy inside the contour Γ, accounted by the first term of the line integral, is caused by the mechanical work done by the traction force acting on the contour Γ, accounted by the second term of the line integral.

Rice demonstrated that: (1) the J-integral is path-independent, which means that its value is independent on the chosen path Γ and (2) the J-integral is equal to the energy release rate G when the LEFM theory holds, thus it can be correlated to the SIF K_i according to Eqs. (28)a-c.

However, Eq. (30) cannot be used to compute the J-integral when dealing with fracture in active materials of LIBs because the chemical and mechanical driving forces are present at the same time. In this case, the J-integral formulated by Rice is no longer path-independent, and the modified expression of the $\hat{J}$-integral, which keeps the path-independence property, is reported in Eq. (31) [28–30].

$$\hat{J} = \int_{\Gamma} \left(\psi_{el} dy - t_i \frac{\partial u_i}{\partial x} \right) ds + \int_{\Lambda} \Omega \sigma_h \frac{\partial c}{\partial x} d\Lambda \tag{31}$$

Where Λ is the area enclosed by Γ. The first term of Eq. (31) is the standard J-integral reported in Eq. (30), whereas the second term accounts for the energy due to the deformation induced by lithium diffusion. Eq. (31) states that the elastic strain energy is no longer the only energy source when considering fracture caused by lithiation and delithiation processes, thus the energy related to diffusion induced deformation needs to be taken into account to satisfy the energy balance and to ensure the path-independence property of $\hat{J}$-integral.

3.1.4. Crack growth

A significant objective of fracture mechanics models is the description of crack growth. Such models aim to calculate:

- the threshold load which initiates crack propagation;
- the direction of crack propagation θ_c;
- the amount of crack propagation Δa.

In addition, an important feature of fracture is the stability of crack propagation. Crack propagation can be classified as unstable or stable. The crack propagation is unstable if the crack grows abruptly without increasing the external load. On the contrary, the crack growth is stable if an additional increase of the external load is necessary to further increase the crack length.

The following sections provide the crack propagation criteria to establish the occurrence and direction of crack propagation, according to static or cyclic loads.

Crack propagation due to static load. When a component is subjected to a static load and a single cracking mode, the corresponding SIF K_i provides the crack propagation criterion. Crack propagation occurs when K_i is greater than the material fracture toughness $K_{i,cr}$, according to Eq. (32).

$$K_i \geq K_{i,cr} \quad \text{Crack propagation} \tag{32}$$

Alternatively, the energetic criterion proposed by Griffith can be employed. The crack propagates when the energy release rate G is greater than the critical energy release rate G_{cr}, which is an intrinsic material parameter.

$$G \geq G_{cr} = 2\gamma_s \quad \text{Crack propagation} \tag{33}$$

Where γ_s is the surface energy, depending on the material.

The crack propagates following the initial orientation when it is subjected to a single cracking mode.

On the other hand, three criteria are used to determine the occurrence and the direction of crack propagation in the case of mixed cracking mode: the criterion of the maximum circumferential stress, the criterion of the maximum energy release rate, and the criterion of the strain energy density.

The criterion of the maximum circumferential stress is the most adopted because of its simplicity and effectiveness, even in commercial FE software, such as Ansys and Abaqus. Then, this criterion is described here, and further details about the other two criteria can be found in a reference textbook [31].

The criterion of the maximum circumferential stress states that crack grows if the circumferential stress σ_c (at a certain distance r_c from the crack tip) reaches a critical material threshold $\sigma_{c,max}$. The circumferential stress at the crack tip is calculated as a function of K_i, where i is the number of present modes, according to Anderson et al. [31]. On the other hand, $\sigma_{c,max}$ is related to the fracture toughness of mode I ($K_{I,cr}$) according to Eq. (34), regardless of the modes present.

$$\sigma_c(r_c, \theta_c) \geq \sigma_{c,max} = \frac{K_{I,cr}}{\sqrt{2\pi r_c}} \quad \text{Mixed-mode crack propagation} \tag{34}$$

The crack propagates in the direction θ_c which maximizes the circumferential stress, according to Eq. (35).

$$\theta_c = 2 \arctan \left[\frac{1}{4} \frac{K_I}{K_{II}} - \frac{1}{4} \sqrt{\left(\frac{K_I}{K_{II}} \right)^2 + 8} \right] \tag{35}$$

Crack propagation due to cyclic loading. When a component is subjected to cyclic loading, micro-cracks arise from the material imperfections, such as voids and micro-defects at first (Stage I). As the fatigue threshold is overcome, these micro-cracks start to propagate stably (Stage II) and then unstably (Stage III), leading to component failure ultimately.

Paris' law is often used to model fatigue crack growth due to cyclic loading. According to Paris' law, the crack growth is described by the SIF range (ΔK), which is defined according to Eq. (36).

$$\Delta K = K_{max} - K_{min} \tag{36}$$

Where K_{max} and K_{min} are the maximum and minimum SIF during the loading cycle, respectively. The crack does not propagate (Stage I) when ΔK is below the fatigue threshold K_{th}, whereas crack propagation becomes unstable when $\Delta K \geq K_{i,cr}$ (Stage III). The stable propagation of the crack (Stage II) is described by Paris' Law, according to Eq. (37) [32–34].

$$\frac{da}{dN} = C(\Delta K)^m \tag{37}$$

Where $\frac{da}{dN}$ is the crack growth rate, N is the number of loading cycles, C and m are material constants determined experimentally.

A modification of Paris' law including the effect of stress ratio $R = \frac{K_{min}}{K_{max}}$ and the limits of threshold and unstable crack propagation regimes is expressed by Eq. (38).

$$\frac{da}{dN} = \frac{C(\Delta K - K_{th})^m}{(1-R)K_{cr} - \Delta K} \tag{38}$$

Active material particles of electrodes experience alternating stress during repeated charge and discharge cycles which may cause the growth of pre-existent defects. Therefore, Paris' law can be applied to account for fatigue crack growth in active material particles under the following assumptions [35–40]:

- The particle is assumed to be spherical.
- All pre-existent cracks are the same and uniformly distributed among particles.
- The number of cracks does not change throughout the battery life, meaning that no crack can initiate during cycling.
- Crack width remains constant and only the crack length a increases during cycling.

In this case, crack propagation under mode I occurs due to the tensile hoop stress σ_c. Substituting the expression of the SIF range (Eq. (39)a) in Eq. (37), Paris' law for fracture in LIBs due to mode I is expressed by Eq. (39)b.

$$\Delta K = K_{max} - K_{min} = (\sigma_{c,max} - \sigma_{c,min})Y\sqrt{\pi a} \tag{39a}$$

$$\frac{da}{dN} = C[(\sigma_{c,max} - \sigma_{c,min})Y\sqrt{\pi a}]^m \tag{39b}$$

Where $\sigma_{c,max}$ and $\sigma_{c,min}$ are the maximum and minimum tensile hoop stress occurring during cycling, respectively.

Alternatively, an equivalent SIF range (ΔK_{eq}) is employed when dealing with mixed-mode crack propagation, according to Eq. (40)a, and Paris' law is reported in Eq. (40)b.

$$\Delta K_{eq} = \frac{1}{2}\cos\left(\frac{\theta_c}{2}\right)\left[\Delta K_I(1+\cos\theta_c) - 3\Delta K_{II}\sin\theta_c\right] \tag{40a}$$

$$\frac{da}{dN} = C\left\{\frac{1}{2}\cos\left(\frac{\theta_c}{2}\right)\left[\Delta K_I(1+\cos\theta_c) - 3\Delta K_{II}\sin\theta_c\right]\right\}^m \tag{40b}$$

Where the direction of crack propagation θ_c is evaluated using Eq. (35).

Paris' law can be solved both numerically or analytically, namely the SIF range can be computed using a FEM or XFEM-based approach or analytically computing the hoop stress and geometric factor Y.

The parameters C and m are empirical coefficients depending on the electrode material and they have to be obtained by performing experimental tests. However, performing experimental measurements is not trivial, and reliable results are still lacking in the literature. Therefore, most of the studies treated C and m as fitting parameters, as it will be further explained in Section 6.

3.2. Phase-field model

The phase-field model (PFM) is used to model crack nucleation and growth and represents a valid alternative to discrete crack models based on LEFM theory. In discrete crack models, cracks are described as geometric features with physical discontinuity. On the other hand, the PFM assumes that the discontinuities introduced by cracks are not sharp, but can be approximated as smeared damage using a continuous parameter, namely the crack phase-field (PF) variable. The continuum approximation of cracks allows addressing some of the numerical challenges of discrete crack models, such as the description of complex crack paths, as well as the inclusion of the effects for crack branching, kinking, or coalescence of multiple cracks without mesh-size influences.

The PFM was initially proposed by Bourdin et al. [41], starting from the variational formulation of Griffith's theory of brittle fracture. Then, it was further developed by Borden et al. [42] and Miehe et al. [43].

The PFM has been successfully used to solve different fracture problems, such as brittle, quasi-brittle, and ductile fracture, even when a significant multi-physics coupling is present, as for fracture in LIBs [44].

The fundamental features and the main equations of the PFM solving fracture in LIBs are discussed below, but further details about the generic implementation of PFM can be found in other reference texts [45–47].

Consider an arbitrary domain $\Omega \subset \mathbb{R}^{n_{dim}}$ ($n_{dim} = 2, 3$), with the external boundary $\partial\Omega \subset \mathbb{R}^{n_{dim}-1}$ and internal crack with corresponding cracked surface $\Gamma \subset \mathbb{R}^{n_{dim}-1}$, as shown in Figure S3.

The total potential energy (Π) of the system is written as the sum of the elastic strain energy (Π_{el}), the fracture energy (Π_Γ) and the energy due to lithium diffusion (Π_{Li}) in Eq. (41), according to Griffith's theory and neglecting inertia effects and external forces.

$$\Pi(\mathbf{u}, c, \Gamma) = \Pi_{el}(\mathbf{u}, c, \Gamma) + \Pi_\Gamma(\Gamma) + \Pi_{Li}(c) = \int_\Omega \psi_{el}(\boldsymbol{\varepsilon_{el}}(\boldsymbol{u}, c))\, d\Omega + \\ + \int_\Gamma G_{cr}\, d\Gamma + \int_\Omega \psi_{Li}(c)\, d\Omega \tag{41}$$

Where ψ_{el} is the elastic strain energy density, G_{cr} is the critical energy release rate, and ψ_{Li} is the chemical energy density due to lithium diffusion.

The elastic strain energy density ψ_{el} is defined in Eq. (42).

$$\psi_{el}(\boldsymbol{\varepsilon_{el}}(\boldsymbol{u}, c)) = \frac{1}{2}\lambda_L[\mathrm{Tr}(\boldsymbol{\varepsilon_{el}})]^2 + \mu_L[\mathrm{Tr}(\boldsymbol{\varepsilon_{el}}^2)] \tag{42}$$

Where λ_L and μ_L are Lamè's first parameter and shear modulus respectively, and $\boldsymbol{\varepsilon_{el}}(\mathbf{u}, c)$ is the elastic strain tensor given by Eq. (43).

$$\boldsymbol{\varepsilon_{el}}(\mathbf{u}, c) = \boldsymbol{\varepsilon}(\mathbf{u}) - \boldsymbol{\varepsilon_{Li}}(c) \tag{43}$$

Where $\boldsymbol{\varepsilon}(\mathbf{u}) = \frac{1}{2}(\nabla\mathbf{u} + (\nabla\mathbf{u}^T))$ is the total strain tensor, $\boldsymbol{\varepsilon_{Li}} = \frac{(c - c_{ref})\Omega}{3}\boldsymbol{I}$ is the chemical strain tensor, $\boldsymbol{u}$ is the displacement field of the body, c_{ref} is the zero-strain concentration and $\boldsymbol{I}$ is the second-order unit tensor.

The chemical energy density ψ_{Li} is expressed in Eq. (44) as a function of the thermodynamic potential (μ). The thermodynamic potential is computed according to Eq. (6)a, choosing the value of γ_{LiS} on the basis of the ideal or non-ideal solution hypothesis.

$$\mu = \frac{\partial\psi_{LiS}(c)}{\partial c} \tag{44}$$

In PFM, the scalar PF variable $d(\boldsymbol{x}) \in [0, 1]$ and length scale parameter l_0 are introduced to avoid the explicit representation of the

crack surface Γ and to approximate the crack as a band of finite thickness. The PF parameter (d) distinguishes the intact from the cracked material, according to the definition reported in Eq. (45).

$$d(\mathbf{x}) = \begin{cases} 0, \text{if the material is intact} \\ 1, \text{if the material is cracked} \end{cases} \tag{45}$$

Where $\mathbf{x}$ is the direction normal to the crack surface.

The key feature of the PFM is that the PF variable (d) varies continuously within the transition region between intact and completely cracked material. The length scale parameter (l_0) controls the width of this transition region, thus determining the area where the PF variable (d) ranges. As l_0 approaches zero, a discontinuous function representing the discrete crack is recovered.

Then, the surface integral of the fracture energy $\Pi_\Gamma(\Gamma)$ in Eq. (41) is substituted with a volume integral defined over the entire domain Ω, according to Eq. (46).

$$\Pi_\Gamma(\Gamma) = \int_\Gamma G_{cr} d\Gamma \approx \Pi_\Gamma(d) = \int_\Omega G_{cr} \chi(d, \nabla d) d\Omega \tag{46}$$

Where $\chi(d, \nabla d)$ is the crack surface density function that considers the amount of damage in the volume Ω. It has the unit of length and allows extending the integral of the crack surface to the volume. A common choice for $\chi(d, \nabla d)$ is reported in Eq. (47) [41].

$$\chi(d, \nabla d) = \left(\frac{d^2}{2l_0} + \frac{l_0}{2} |\nabla d|^2 \right) \tag{47}$$

The gradual degradation of the material stiffness caused by the crack propagation can be taken into account by coupling the expression of the elastic strain energy density ψ_{el} reported in Eq. (42) with the PF variable (d), using a degradation function $g(d)$. Therefore, the elastic strain energy density affected by degradation ($\widetilde{\psi}_{el}(\mathbf{u}, c, d)$) is expressed according to Eq. (48), giving rise to the so-called isotropic PFM.

$$\widetilde{\psi}_{el}(\mathbf{u}, c, d) = g(d) \psi_{el}(\mathbf{u}, c) \tag{48}$$

The degradation function $g(d)$ monotonically decreases as the PF variable (d) increases, and satisfies $g(0) = 1$ and $g(1) = 0$. A common expression of $g(d)$ is reported in Eq. (49) [41].

$$g(d) = (1 - d)^2 \tag{49}$$

The isotropic PFM allows crack propagation in regions subjected to compressive stress, thus causing nonphysically crack evolution paths. To address this issue, Amor et al. [48] and Miehe et al. [49] proposed an anisotropic PFM that splits the elastic energy density into tension and compression contributions. Then, the degradation function ($g(d)$) is applied only to the tensile part of the elastic strain energy density, according to Eq. (50).

$$\widetilde{\psi}_{el}(\mathbf{u}, c, d) = g(d) \psi^+_{el}(\mathbf{u}, c) + \psi^-_{el}(\mathbf{u}, c) \tag{50}$$

Where ψ^+_{el} and ψ^-_{el} are the tensile and compressive contributions of the elastic strain energy density and their definitions depend on the type of energy split criterion adopted [45]. The approximated total potential energy $\Pi(\mathbf{u}, c, d)$ according to the anisotropic PFM is expressed in Eq. (51), replacing $\psi_{el}(\mathbf{u}, c)$ with $\widetilde{\psi}_{el}(\mathbf{u}, c, d)$ (Eq. (50)) and $\Pi_\Gamma(\Gamma)$ with $\Pi_\Gamma(d)$ (Eq. (46)) in Eq. (41).

$$\begin{aligned} \Pi(\mathbf{u}, c, \Gamma) \approx \Pi(\mathbf{u}, c, d) = & \int_\Omega \left[g(d) \psi^+_{el}(\mathbf{u}, c) + \psi^-_{el}(\mathbf{u}, c) \right] d\Omega + \\ & + \int_\Omega \left[G_{cr} \gamma(d, \nabla d) \right] d\Omega + \int_\Omega \psi_{Li}(c) d\Omega \end{aligned} \tag{51}$$

At this stage, the governing equations for displacement, PF variable, and concentration can be obtained by writing the Lagrangian $L(\mathbf{u}, \dot{\mathbf{u}}, c, d)$ of the system and finding a stationarity point $\delta L = 0$. The Lagrangian of the system can be expressed as the difference between the kinetic energy $E_k(\dot{\mathbf{u}})$ and the total potential energy $\Pi(\mathbf{u}, c, d)$ (Eq. (51)), according to Eq. (52):

$$\begin{aligned} L(\mathbf{u}, \dot{\mathbf{u}}, c, d) = E_k - \Pi = & \int_\Omega \frac{1}{2} \rho \dot{\mathbf{u}} \cdot \dot{\mathbf{u}} - \int_\Omega \left[g(d) \psi^+_{el}(\mathbf{u}, c) \psi^-_{el}(\mathbf{u}, c) \right] d\Omega + \\ & - \int_\Omega \left[G_{cr} \gamma(d, \nabla d) \right] d\Omega + \\ & - \int_\Omega \psi_{Li}(c) d\Omega \end{aligned} \tag{52}$$

Then, the Euler–Lagrange equations of displacement ($\mathbf{u}$) and PF variable (d) are obtained in Eq. (53) finding the stationary point of Eq. (52) ($\delta L = 0$), adopting the crack surface density $\chi(d, \nabla d)$ and degradation functions expressed in Eqs. (47) and (49) respectively, and assuming quasi-static condition ($\ddot{\mathbf{u}} = 0$). Eq. (53)a is the standard equilibrium equation, and Eq. (53)b describes the evolution of the PF variable (d).

$$\nabla \cdot [\boldsymbol{\sigma}(\mathbf{u}, d)] = 0, \tag{53a}$$

$$G_{cr} \left(\frac{d}{l_0} - l_0 \Delta d \right) + 2(d - 1) \psi^+_{el}(\mathbf{u}, c) = 0 \tag{53b}$$

Where the degraded stress tensor $\boldsymbol{\sigma}(\mathbf{u}, d)$ is written in Eq. (54).

$$\boldsymbol{\sigma} = g(d) \frac{\partial \psi^+_{el}}{\partial \boldsymbol{\varepsilon}_{el}} + \frac{\partial \psi^-_{el}}{\partial \boldsymbol{\varepsilon}_{el}} = (1 - d)^2 \frac{\partial \psi^+_{el}}{\partial \boldsymbol{\varepsilon}_{el}} + \frac{\partial \psi^-_{el}}{\partial \boldsymbol{\varepsilon}_{el}} \tag{54}$$

The reduction of the crack length when ψ^+_{el} decreases, such as during the unloading phase, is avoided by adding the irreversibility constraint in Eq. (53)b, according to the approach of Miehe et al. [43]. Thus, ψ^+_{el} in Eq. (53)b is replaced with the so-called local history field $\mathcal{H}$, as reported in Eq. (55).

$$G_{cr} \left(\frac{d}{l_0} - l_0 \Delta d \right) + 2(d - 1) \mathcal{H} = 0 \tag{55}$$

Where $\mathcal{H}$ is defined as the maximum tensile contribution of the elastic energy density function according to Eq. (56).

$$\mathcal{H}(\mathbf{x}, t) := \max_{d \in [0, t]} \psi^+_{el} \tag{56}$$

Although the anisotropic formulation prevents crack growth across compressive regions, it leads to nonlinear equilibrium equations, thus to a more expensive numerical computation. Ambati et al. [50] solved this issue developing the hybrid PFM, which has a linear equilibrium equation. Therefore, the equilibrium equation is taken from the isotropic PFM, replacing $\boldsymbol{\sigma}(\mathbf{u}, d)$ in Eq. (54) with $\boldsymbol{\sigma}(\mathbf{u}, d) = g(d) \frac{\partial \psi_{el}}{\partial \boldsymbol{\varepsilon}_{el}} = (1 - d)^2 \frac{\partial \psi_{el}}{\partial \boldsymbol{\varepsilon}_{el}}$, whereas Eq. (53)b does not change.

Finally, the lithium ion concentration (c) is governed by the transport equation, expressed by Eqs. (18), (20) or (22) in 2, according to the non-ideal coupled, ideal coupled or ideal uncoupled solution model, respectively.

Thus, the complete set of governing equations in the strong form solving the fracture problem in LIBs with the PFM are obtained by combining Eq. (53)a (equilibrium), Eq. (55) (PF evolution) and Eq. (18), (20) or (22) (lithium ion transport), as resumed in Eq. (53).

A well-defined set of boundary conditions is given by $\mathbf{u} = \bar{\mathbf{u}}$ on $\partial\Omega_u$ and $\boldsymbol{\sigma} \cdot \mathbf{n} = \bar{\mathbf{t}}$ on $\partial\Omega_t$ for the equilibrium equation, and $\nabla \cdot d = 0$ and

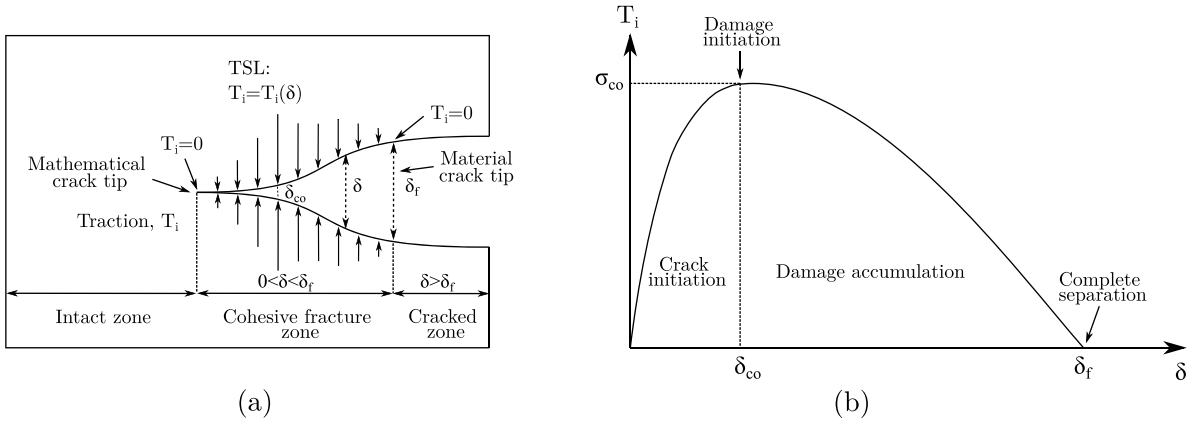

Fig. 2. (a) Sketch of the CZM domains. (b) Generic TSL for single-mode fracture.

$d = 0$ on $\partial\Omega$ for the evolution of the PF variable. Finally, the initial conditions are $c(\mathbf{x}, t_0) = c_0$ and $\mathbf{u}(\mathbf{x}, t_0) = \mathbf{u_0}$.

$$
\begin{cases}
\textbf{Equilibrium} \\
\nabla \cdot [\boldsymbol{\sigma}(\mathbf{u}, d)] = 0, \\
\mathbf{u} = \bar{\mathbf{u}} \qquad \text{on } \partial\Omega_u \\
\boldsymbol{\sigma} \cdot \mathbf{n} = \bar{\mathbf{t}} \qquad \text{on } \partial\Omega_t \\
\textbf{PF evolution} \\
G_{cr}\left(\frac{d}{l_0} - l_0 \Delta d\right) + 2(d-1)\mathcal{H} = 0, \\
\nabla \cdot d = 0 \qquad \text{on } \partial\Omega \\
d = 0 \qquad \text{on } \partial\Omega \\
\textbf{Lithium ion transport} \\
\frac{\partial c}{\partial t} = D c_{max}\left[\left(\frac{2}{r}\alpha + \frac{2}{r}x_{LiS}k + \frac{\partial \alpha}{\partial r}\right)\frac{\partial x_{LiS}}{\partial r} + \right. \\
\left. + k\left(\frac{\partial x_{LiS}}{\partial r}\right)^2 + (\alpha + k x_{LiS})\frac{\partial^2 x_{LiS}}{\partial r^2}\right], \\
\left.\frac{\partial c(r,t)}{\partial r}\right|_{r=R} = N_{surface}(t), \qquad \text{for } t \geq 0 \\
\left.\frac{\partial c(r,t)}{\partial r}\right|_{r=0} = 0, \qquad \text{for } t \geq 0
\end{cases}
\tag{57}
$$

3.3. Cohesive zone model

The cohesive zone model (CZM) overcomes the limits of the LEFM theory as it allows modeling fracture even when the size of the non-linear zone near the crack tip is not negligible as compared to the crack dimension, and without assuming the presence of an initial crack [51].

CZM models fracture as a gradual phenomenon, which occurs in the so-called cohesive fracture zone in front of the crack tip. Referring to Fig. 2a and considering a single-mode fracture, the crack region is divided into three parts: (a) the intact zone loaded by nominal stress, (b) the cohesive fracture zone which is loaded by the cohesive traction T_i (where the subscript i refers to pure fracture mode I, II or III), (c) the cracked zone which is stress-free. The cohesive traction T_i joins together the crack surfaces and depends on the distance between the crack surfaces (δ). The relation between the cohesive traction T_i and δ is the so-called traction separation law (TSL), represented in Fig. 2b.

Fracture consists of the initiation and propagation of the crack caused by the opening and advance of the cohesive zone in front of the crack tip. The main idea is that infinite stress at the crack tip is not realistic. Thus, the crack tip singularity is removed by considering that the stress in the cohesive zone cannot overcome the cohesive strength of the material σ_{co} (refer to Fig. 2b). Indeed, when the cohesive traction reaches σ_{co}, it decreases and drops to zero when δ reaches the critical value δ_f. At this stage, the complete separation occurs and new crack surfaces are generated (Fig. 2a-b).

The TSL law is expressed according to Eq. (58) and depends on the material.

$$T_i = T_i(\delta_i) \tag{58}$$

The area under the cohesive law curve represents the so-called cohesive energy $\Gamma_{c,i}$, i.e. the energy required for the separation of crack surfaces, expressed in Eq. (59).

$$\Gamma_{c,i} = \int_0^{\delta_{f,i}} T_i(\delta_i) d\delta_i \tag{59}$$

The cohesive energy is equal to the Griffith critical energy release rate if there is no energy dissipation around the crack.

Different TSLs exist in the literature, based on the type of material and separation mechanism, such as triangle, bilinear, linear–parabolic and exponential. Table S5 summarizes the most popular TSL with their corresponding equations and a brief description of their applications [52–57]. The bilinear law is the most used TSL to model fracture in LIBs.

The quadratic stress criterion in Eq. (60) is adopted to define the damage initiation when the material is subjected to mixed-mode loading.

$$\left(\frac{T_I}{\sigma_{co,I}}\right)^2 + \left(\frac{T_{II}}{\sigma_{co,II}}\right)^2 + \left(\frac{T_{III}}{\sigma_{co,III}}\right)^2 = 1 \tag{60}$$

Where $\sigma_{co,i}$ is the cohesive strength for the mode i. Then, an equivalent separation δ_{eq} is computed according to Eq. (61), considering the contribution of all the modes.

$$\delta_{eq} = \sqrt{\delta_I^2 + \delta_{II}^2 + \delta_{III}^2} \tag{61}$$

The complete separation, which occurs when the cohesive energy of mode i ($\Gamma_{c,i}$) equals the corresponding energy release rate G_i in the case of single mode, is defined by the following mixed-mode criterion:

$$\left(\frac{G_I}{\Gamma_{c,I}}\right)^{\alpha_{co}} + \left(\frac{G_{II}}{\Gamma_{c,II}}\right)^{\alpha_{co}} + \left(\frac{G_{III}}{\Gamma_{c,III}}\right)^{\alpha_{co}} = 1 \tag{62}$$

Where α_{co} is an empiric value, usually ranging between 1 and 1.6 and defined through experimental tests [58].

3.4. Concluding remarks

The fundamentals fracture mechanics model are reviewed in this section. In particular, the followings are remarked:

Table 2
Summary of the main works existing in the literature using the weight function method to compute K_I in LIBs. Coupling refers to the mechanical–diffusive coupling explained in Section 2.

Particle geometry	Crack geometry	Electrode material	Coupling	Ref.
Spherical	Superficial crack	LMO	No	[59]
Spherical	Superficial crack	LMO	No	[60]
Spherical	Superficial crack	LMO	Yes	[61]
Spherical	Edge crack on phases interface	LFP	Yes	[62]
Spherical	Radial crack	Silicon	No	[63]

- LEFM assumes that the plastic area near the crack tip is negligible compared to the crack dimension. The stress at the crack tip is computed with the SIF, which is also a parameter used to determine if the crack can propagate, both due to static and cyclic loads according to proper criteria. Therefore, the LEFM model is applied when the material behavior near the crack tip is linear elastic and, compared to the other fracture models, it cannot describe the fracture in non-linear and plastic materials. Furthermore, a pre-existent crack is needed, thus it is not possible to model the crack initiation stage. On the other hand, compared to other fracture models, analytical solutions based on LEFM theory in the case of simple geometries and loading conditions are available.
- PFM is an energetic approach and it can be viewed as the generalization of Griffith's theory of LEFM. Unlike other fracture models, the PF variable d, ranging from 0 (intact material) to 1 (broken material), avoids the explicit representation of the crack and eliminates the geometrical discontinuities in the model. For this reason, the PFM is an effective approach to model fracture in the case of complex geometries and loading conditions compared with the traditional approach of LEFM or the CZM model. Furthermore, unlike the LEFM model, the PFM can be applied without assuming pre-existent cracks.
- CZM allows modeling both elastic and plastic materials, with respect to the previous models. The non-physical stress singularity at the crack tip is eliminated by assuming that the stress cannot overcome the threshold value of the cohesive strength. The opening of the crack is evaluated on the basis of the TSL, depending on the material. After the cohesive strength is overcome, the cohesive traction, which binds the two faces of the crack, decreases as long as the crack opens and finally drops to zero, resulting in the crack extension. Unlike the LEFM and PFM models, the CZM is based on the cohesive law to model the fracture behavior of the material, which is difficult to be obtained experimentally, limiting the reliability of the results.

4. Numerical implementation of fracture mechanical models applied to LIBs

The numerical implementation of the fracture models for LIBs covered in Section 3 is described in this Section. The propagation of a crack in active material particles of electrodes leads to a significant discontinuity in the displacement and stress fields. Dealing with this discontinuity is cumbersome from the modeling point of view and different numerical methods have been proposed in literature over the years. Some models follow a discrete approach and deal with discontinuity, others follow a continuum approach to work around the problem. Furthermore, crack propagation is in general simulated numerically, and the analytical approach can be used only in the case of simple geometry and loading conditions.

4.1. Analytical

The analytical approach can be used to solve the fracture problem only for simple geometry and loading conditions. In this case, tabulated geometric factor (Y) is often employed to compute the SIF (K) [64–66], according to Eq. (23). However, closed-form solutions for K are not directly available for arbitrary cracks in complex structures or under complex loading conditions, such as for cracks in LIBs. In this case, the weight function method can be employed to compute K.

Then, Eq. (32) is employed to evaluate crack propagation due to a single (de)lithiation, once the SIF is computed. Alternatively, Paris' law expressed in Eq. (37) is used to model the crack growth due to repeated charge/discharge cycles.

4.1.1. Weight function method

The SIF (K) due to an arbitrary load is computed using a weight function w obtained from a simpler load case, taken as a reference. The weight function w does not depend on the stress distribution and is known for the geometry of the model of interest. Practically, the SIF is computed by multiplying the weight function w by the arbitrary stress distribution and integrating along the crack length, as expressed in Eq. (63).

$$K = \int_0^a \sigma(x) w(x,a) dx \tag{63}$$

Where $\sigma(x)$ is the stress distribution normal to the crack surface in the uncracked body, $w(x,a)$ is the weight function, x is the coordinate parallel to the crack direction and a is the crack length. The weight function w is computed from a reference case, according to Eq. (64).

$$w(x,a) = \begin{cases} \dfrac{E}{K_{\text{ref}}} \dfrac{\partial u_{\text{ref}}(x,a)}{\partial a} & \text{plane stress} \\ \dfrac{E}{(1-\nu^2)K_{\text{ref}}} \dfrac{\partial u_{\text{ref}}(x,a)}{\partial a} & \text{plane strain} \end{cases} \tag{64}$$

Where K_{ref} and $u_{\text{ref}}(x,a)$ are the reference SIF and the corresponding displacement at the crack tip, respectively.

Some works used the weight function method to compute the mode I SIF (K_I) due to the hoop stress arising in spherical active material particles during lithium insertion and extraction. A summary of the feature of the models is given in Table 2.

The effect of mechanical–diffusive coupling was neglected in earlier works, such as [59,60,63]. However, the most recent works, such as [61,62], computed the hoop stress with a coupled mechanical–diffusive model.

Different electrode materials and crack geometries were modeled, such as $LiMn_2O_4$ (LMO) [59–61], $LiFePO_4$ (LFP) [62] and Silicon [63], superficial cracks [59–61], edge cracks on the phases interface [62] and radial cracks [63].

K_{ref} and u_{ref} were obtained from an approximated geometry since they are not available for the geometry of the particle. For example, the spherical particles with superficial crack in [59] and radial crack in [63] were approximated as equivalent plates with semielliptical edge cracks, whereas the spherical particles with superficial crack in [61] and crack at phases interface in [62] were approximated as circular disks with edge cracks. Clearly, this approximation may affect the accuracy of the K_I computation. This is the reason why numerical approaches are often preferred to compute the SIF.

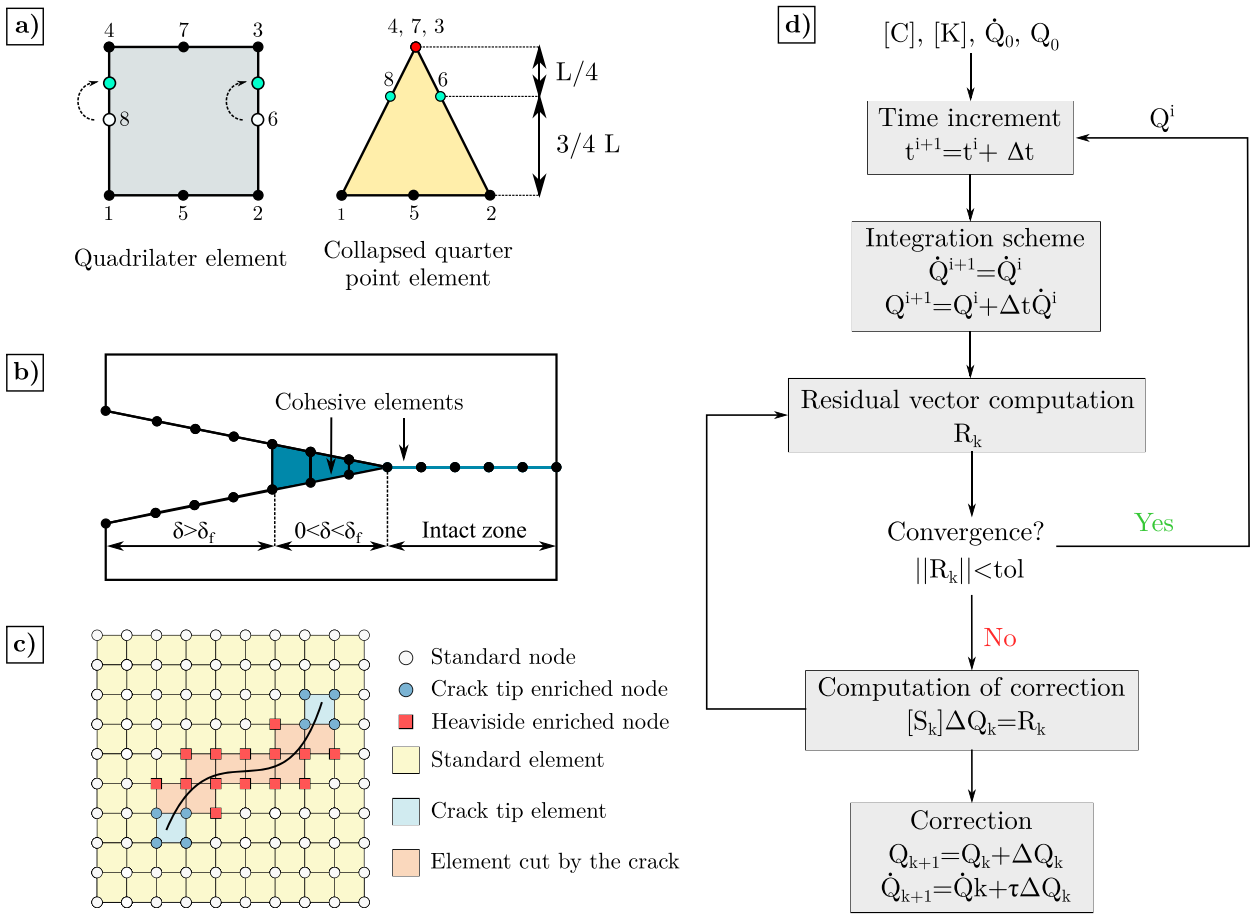

Fig. 3. (a) Collapsed quarter point elements for 2D model. Standard 8-nodes quadrilateral elements are represented on the left and collapsed quarter point elements are represented on the right. (b) Crack growth modeling with CZM. Cohesive elements are depicted in blue and join together the crack surface according to the TSL. When $\delta < \delta_{co}$, the material is undamaged, whereas the damage accumulates irreversibly as $\delta > \delta_{co}$, then the stiffness of cohesive elements decreases, as well as the cohesive traction. When the failure separation δ_f is reached, the traction drops to zero, the cohesive element is deleted, and the crack is formed. (c) Typical XFEM mesh of a cracked body. The nodes of the elements cut by the crack are represented by red squares and are enriched with the Heaviside functions, whereas the nodes at the crack tip are represented by blue circles and are enriched with the crack tip asymptotic functions. (d) Flowchart of the Newton–Raphson method to solve PFM Equations for fracture in LIBs. (For interpretation of the references to color in this figure legend, the reader is referred to the web version of this article.)

4.2. FEM

FEM is generally employed to solve more complex crack problems since closed-form solutions of SIF (K) exist only for a few simple crack configurations and loading conditions. Thus, FEM represents a valid alternative to the analytical approach to model fracture in LIBs due to single (de)lithiation, as well as repeated cycles.

4.2.1. Mesh

The main issue is the representation of the singularity of displacement and stress fields at the crack tip because the polynomials used to approximate the solution are not able to reproduce the $1/\sqrt{r_c}$ singularity at the crack tip.

Barsoum et al. [67] showed that the singularity of the stress field can be accurately modeled using the so-called collapsed quarter point elements. These elements are obtained by collapsing one side (the one containing the nodes 4, 7, 3 on the left in Fig. 3a) to a single point (located at the crack tip and represented in red on the right in Fig. 3a), and shifting the mid-side nodes near the crack tip to a quarter position (the nodes 6 and 8 represented in green on the right in Fig. 3a). Collapsed quarter point elements are frequently employed in crack simulations and they are implemented in several commercial FE software, such as ANSYS, ABAQUS, and COMSOL.

4.2.2. Numerical implementation

The fracture mechanics models presented in Section 3 (LEFM and CZM) have been implemented using FEM to compute crack growth.

LEFM. Fracture parameters, such as SIF, energy release rate G or J-integral are computed at each time step of the simulation. The fracture criteria summarized in Section 3.1.4 are used to determine the occurrence and direction of crack propagation due to static loading. On the other hand, Paris' law is often employed to simulate fatigue crack growth. In this case, the SIF range $\Delta K = K_{max} - K_{min}$ is computed numerically for the maximum load. Then, the number of cycles required to increase the crack length of a fixed Δa is estimated through Paris' law expressed in Eq. (37).

Once the crack propagates due to static or cyclic loading, the crack geometry and mesh are updated, considering that the crack increment Δa is usually predefined and kept fixed during the simulation. Then, the procedure described above is repeated for the successive time step or cycle.

Re-meshing generally consists of four steps: (1) the existing mesh around the crack is removed; (2) the geometry of the crack is modified according to the determined crack length increment and direction; (3) quarter-point elements are created around the crack tip; (4) a new mesh is generated in the remained not meshed area.

Re-meshing is highly cumbersome, especially if the model is 3D and the geometry and the crack path are complex and not known

Table 3
Summary of the main works existing in the literature using CZM in FEM framework to model fracture in electrode active materials.

Active material	Geometry	Goals	Operation	Chemo-mechanical coupling	Ref.
Graphite	Anisotropic cylindrical particle	Analysis of the location and orientation dependent crack propagation	Cycling charging	Yes	[73]
NMC	Spherical particle made of several primary particles	Intergranular cracking simulation	Single charge/discharge cycle	No	[68]
NMC	Spherical particle made of several primary particles	Intergranular cracking simulation including the effect of lithium embrittlement on crack propagation	Cyclic charge/discharge cycles	Yes	[74]
NMC	Spherical particle made of several primary particles	Intergranular cracking simulation to assess the influence of the fracture energy	Single and cyclic charge/discharge cycles	No	[69]
NMC	Spherical particle made of several primary particles	Intergranular cracking simulation to assess the influence of primary particle sizes, regularities, interfacial strength, current rates and fracture energy	Single charge/discharge cycle	No	[71,72]
LMO	Thin film polycrystalline	Development of a coupled mechanical-diffusive CZM fracture model	Single charge/discharge cycle	Yes	[75]
NMC	Spherical particle made of primary particles	Development of a coupled mechanical–diffusive CZM model which estimates intergranular cracking and its influence on lithium transport	Single discharge	Yes	[70]

in advance. In addition, modeling fracture in LIBs requires solving a multiphysics problem which further increases the computational effort of the simulation. For this reason, this kind of approach is not widely employed in literature, whereas other numerical methods, such as the XFEM or the PFM, are preferred.

Cohesive zone model. In contrast to LEFM theory, no pre-existent cracks and singular elements at the crack tip are needed in the CZM, and both brittle and ductile fractures can be simulated.

A layer composed of zero-thickness cohesive elements is introduced at the interface between standard elements, in the areas where the crack is supposed to propagate. Material damage and separation occur only within the cohesive elements layer, whereas the surrounding standard elements are damage-free.

Cohesive elements apply a traction force which joins the adjacent standard elements based on the specific TSL. The damage starts to accumulate irreversibly when the stress within the element exceeds the cohesive strength σ_{co}, thus the cohesive elements lose their stiffness, as the traction decreases according to the TSL. Finally, traction drops to 0 when the fracture separation δ_f is reached, then standard elements are disconnected and the crack increment occurs (Fig. 3b).

The CZM was employed as an alternative to the LEFM to study the crack propagation in electrode active materials due to single (de)lithiation [68–72], as well as repeated charge/discharge cycles [68,71,72]. Table 3 summarizes the main works existing in the literature.

The main drawback of the CZM implemented in the FEM framework is that re-meshing is still necessary when the crack path is not known in advance because the crack can propagate only along the cohesive elements layer. Furthermore, the CZM requires some material parameters, such as cohesive strength σ_{co}, fracture separation δ_f and cohesive energy Γ_c, which are still difficult to determine.

4.3. XFEM

The extended finite element method (XFEM) is based on the Partition of Unit Method (PUM) [76] and represents a valid alternative to overcome the issues associated with the standard FEM-based modeling of fracture. Indeed, the XFEM method does not require a conforming mesh to obtain a good estimation of the stress and displacement singularity at the crack tip, being suitable to simulate an unknown and complex crack growth path.

The reader can refer to specific works available in the literature, as [77,78] for a more general and detailed explanation of the XFEM method.

The XFEM method adopts a uniform mesh neglecting the geometric discontinuity introduced by the crack. The so-called enriched functions $F_e(\boldsymbol{x})$ are used to estimate the singularity of the solution at the crack tip. Therefore, all the nodes of the elements cut by the crack are enriched with additional degrees of freedom as compared to the standard FEM, as depicted in Fig. 3c.

The general expression of the enriched displacement $\boldsymbol{u^h}(\boldsymbol{x})$ is reported in Eq. (65).

$$\boldsymbol{u^h}(\boldsymbol{x}) = \sum_{i \in \mathcal{N}} N_i(\boldsymbol{x})\hat{\boldsymbol{u}}_i + \sum_{j \in \mathcal{N}^{enr}} N_j(\boldsymbol{x})(F_e(\boldsymbol{x}) - F_e(\boldsymbol{x}_j))\hat{\boldsymbol{a}}_j \tag{65}$$

Where $\mathcal{N}$ is the set of all nodes of the FE mesh, $\mathcal{N}^{enr}$ is the set of enriched nodes, $N_i(\boldsymbol{x})$ is the standard shape function for node i, $\hat{\boldsymbol{u}}_i$ is the standard nodal displacement vector, $N_j(\boldsymbol{x})$ is the standard shape function for the enriched node j, $F_e(\boldsymbol{x})$ is the enrichment function and $F_e(\boldsymbol{x}_j)$ is its value at the node j, x_j is the spatial coordinate of the node j and $\hat{\mathbf{a}}_j$ is the enriched displacement of node j.

Two types of enrichment functions are commonly used in the LEFM theory, namely the Heaviside jump function and the asymptotic crack tip function.

The Heaviside jump function is expressed in Eq. (66) and allows modeling the discontinuity in the displacement field due to the crack. All the nodes of the elements cut by the crack are enriched with the Heaviside jump function.

$$H(\boldsymbol{x}) = \begin{cases} 1, \text{above the crack} \\ -1, \text{below the crack} \end{cases} \tag{66}$$

The asymptotic crack tip function is used to enrich the degrees of freedom of the node at the crack tip to properly describe the singularity

of the displacement field, according to Eq. (67).

$$F(r_c,\theta) = \{F_1, F_2, F_3, F_4\} = \\ = \{\sqrt{r_c}\sin\frac{\theta}{2}, \sqrt{r_c}\cos\frac{\theta}{2}, \sqrt{r_c}\sin\frac{\theta}{2}\cos\frac{\theta}{2}, \sqrt{r_c}\cos\frac{\theta}{2}\sin\theta\} \quad (67)$$

Where r_c and θ are spatial coordinates of a polar system with the origin at the crack tip.

The enriched displacement $\boldsymbol{u}^h$ expressed in Eq. (65) can be rewritten substituting the enriched functions expressed in Eqs. (66) and (67), obtaining the standard XFEM approximation of the displacement field reported in Eq. (68).

$$\boldsymbol{u}^h(\boldsymbol{x}) = \sum_{i\in\mathcal{N}} N_i(\boldsymbol{x})\hat{\boldsymbol{u}}_i + \sum_{j\in\mathcal{N}^{dis}} N_j(\boldsymbol{x})(H(\boldsymbol{x}) - H(\boldsymbol{x}_j))\hat{\boldsymbol{h}}_j \\ + \sum_{k\in\mathcal{N}^{tip}} N_k(\boldsymbol{x}) \sum_{\alpha=1}^{4} (F_\alpha(\boldsymbol{x}) - F_\alpha(\boldsymbol{x}_k))\hat{\boldsymbol{f}}_{\alpha k} \quad (68)$$

Where $\mathcal{N}$ is the set of all nodes of the mesh, $\mathcal{N}^{dis}$ is the set of nodes of elements cut by the crack and enriched by the Heaviside function, $\mathcal{N}^{tip}$ is the set of nodes of the elements containing the crack tip and enriched by the asymptotic functions, $\hat{\boldsymbol{u}}_i$ is the standard nodal displacement vector, $\hat{\boldsymbol{h}}_j$ is the enriched displacement nodal vector associated with the Heaviside enrichment function at node j, $\hat{\boldsymbol{f}}_{\alpha k}$ is the enriched displacement nodal vector associated with the asymptotic functions at node k.

The XFEM can include other fracture models in addition to LEFM, such as the CZM. In this case, only the Heaviside enrichment function is employed and the crack tip nodes are not enriched since the singularity in the displacement field is no longer present. On the other hand, cohesive elements and TSL are employed similarly to the standard FEM.

The XFEM can be used to model crack propagation in LIBs both during single (de)lithiation [79–81] and repeated cycles, following the same procedure described in Section 4.2 for the standard FEM. The only difference is that re-meshing is not necessary, and just the enrichment of nodes of elements cut by the crack needs to be updated based on the crack tip position.

4.4. Phase-field model

The set of governing equations reported in (53) solving fracture mechanics in LIBs according to PFM constitutes a system of coupled non-linear partial differential equations (PDEs) in the unknown fields $\mathbf{u}$, c and d. These equations are solved numerically according to the FE discretization.

First, the system of Equations in (53) is formulated in the weak form, as reported in Eq. (69). For the sake of clarity, the ideal solution with the coupled model is adopted in (69)c.

$$\int_\Omega \delta\mathbf{u}(\nabla\cdot[g(d)\boldsymbol{\sigma}])d\Omega = 0 \quad (69a)$$

$$\int_\Omega \left[G_{cr}\left(\frac{d\delta d}{l_0} + l_0\nabla d\cdot\nabla\delta d\right) - 2(1-d)\mathcal{H}\delta d\right] d\Omega = 0 \quad (69b)$$

$$\int_\Omega \left(\delta c\frac{\partial c}{\partial t} + D\nabla c\cdot\nabla\delta c - \frac{D\Omega c}{RT}\nabla\sigma_h\delta c\right) d\Omega = 0 \quad (69c)$$

Where $\delta\mathbf{u}$, δd and δc are the test functions for the displacement field ($\mathbf{u}$), PF variable (d), and concentration (c), respectively.

Then, the weak form in Eq. (69) is discretized according to FEM, approximating $\mathbf{u}$, d and c with shape functions according to their nodal values, as reported in Eq. (70).

$$\mathbf{u} = \sum_i^n N_i\hat{\mathbf{u}}_i, \quad d = \sum_i^n N_i\hat{d}_i, \quad c = \sum_i^n N_i\hat{c}_i \quad (70)$$

Where $\hat{\mathbf{u}}_i$, $\hat{d}_i$, $\hat{c}_i$ are the nodal values of the displacement, PF and concentration respectively, n is the total number of nodes per element and N_i is the corresponding shape function. The strain and gradient terms are approximated according to Eq. (71).

$$\boldsymbol{\varepsilon} = \sum_i^n [\mathbf{B}_i^u]\hat{\mathbf{u}}_i, \quad \nabla d = \sum_i^n [\mathbf{B}_i]\hat{d}_i, \quad \nabla c = \sum_i^n [\mathbf{B}_i]\hat{c}_i \quad (71)$$

Where the matrices $[\mathbf{B}_i^u]$ and $[\mathbf{B}_i]$, expressed in Eq. (72), are the derivative of the shape functions.

$$[\mathbf{B}_i]^u = \begin{bmatrix} \frac{\partial N_i}{\partial x} & 0 & 0 \\ 0 & \frac{\partial N_i}{\partial y} & 0 \\ 0 & 0 & \frac{\partial N_i}{\partial z} \\ \frac{\partial N_i}{\partial y} & \frac{\partial N_i}{\partial x} & 0 \\ 0 & \frac{\partial N_i}{\partial z} & \frac{\partial N_i}{\partial y} \\ \frac{\partial N_i}{\partial z} & 0 & \frac{\partial N_i}{\partial x} \end{bmatrix}, \quad [\mathbf{B}_i] = \begin{bmatrix} \frac{\partial N_i}{\partial x} \\ \frac{\partial N_i}{\partial y} \\ \frac{\partial N_i}{\partial z} \end{bmatrix} \quad (72)$$

The stress tensor $\hat{\boldsymbol{\sigma}}$ is approximated according to Eq. (73).

$$\hat{\boldsymbol{\sigma}} = \sum_i^n [\mathbf{C}_0]\left\{[\mathbf{B}_i^u]\hat{\mathbf{u}}_i - N_i\hat{c}_i\frac{\Omega}{3}[\boldsymbol{I}]\right\} \quad (73)$$

Where $[\mathbf{C}_0]$ is the linear elastic stiffness matrix or elastic moduli, $[\mathbf{I}]$ is the identity matrix.

Then, the governing equations (Eq. (69)a-c) are written as a function of nodal values with Eqs. (70), (71) and (73). The resulting system of equations is expressed in Eqs. (74)a-c.

$$\int_\Omega g(d)[\mathbf{B}_i^u]^T\hat{\boldsymbol{\sigma}}d\Omega = \mathbf{R}_i^u = 0 \quad (74a)$$

$$\int_\Omega \left[G_{cr}\left(\frac{\hat{d}N_i}{l_0} + l_0[\mathbf{B}_i]^T\nabla\hat{d}\right) - 2(1-\hat{d})\mathcal{H}N_i\right] d\Omega = R_i^d = 0 \quad (74b)$$

$$\int_\Omega \left(N_i\frac{\partial c}{\partial t} + [\mathbf{B}_i]^T D\nabla\hat{c} - [\mathbf{B}_i]^T\frac{D\Omega\hat{c}^n}{RT}\nabla\hat{\sigma_h}\right) d\Omega = R_i^c = 0 \quad (74c)$$

Where $\mathbf{R}_i^u$, R_i^d and R_i^c is the residual vector of $\mathbf{u}$, d and c, respectively.

The aim is to find a value of $\mathbf{Q} = \{\boldsymbol{u}, d, c\}$ so that $\mathbf{R}(\mathbf{Q}) = \left[\mathbf{R}_i^u(\mathbf{u}), R_i^d(d), R_i^c(c)\right] = [\mathbf{0}, 0, 0]$. Since Eqs. (74)a-c are coupled and non-linear, then the Newton–Raphson method is used to solve them iteratively.

First, an initial guess solution $\mathbf{Q}_1$ is considered. If $\mathbf{R}(\mathbf{Q}_1) \neq 0$, it is necessary to find $\Delta\mathbf{Q}_1$ so that $\mathbf{R}(\mathbf{Q}_1 + \Delta\mathbf{Q}_1) \approx 0$. $\mathbf{R}(\mathbf{Q}_1 + \Delta\mathbf{Q}_1)$ is expressed according to Eq. (75) using Taylor series.

$$\mathbf{R}(\mathbf{Q}_1 + \Delta\mathbf{Q}_1) = \mathbf{R}(\boldsymbol{Q}_1) + [\mathbf{S}(\boldsymbol{Q}_1)]\Delta\mathbf{Q}_1 \quad (75)$$

Where $[\mathbf{S}(\boldsymbol{Q}_1)]$ is the iteration matrix, which is defined according to Eq. (76).

$$[\mathbf{S}(\boldsymbol{Q}_1)] = \left.\frac{\partial\mathbf{R}}{\partial\mathbf{Q}}\right|_{\mathbf{Q}_1} \quad (76)$$

The increment $\Delta\boldsymbol{Q}_1$ which would make $\mathbf{R}(\mathbf{Q}_1 + \Delta\mathbf{Q}_1)$ equal to zero is computed with Eq. (77)a and added to the solution according to Eq. (77)b.

$$[\mathbf{S}(\mathbf{Q}_1)]\Delta\mathbf{Q}_1 = -\mathbf{R}(\mathbf{Q_1}) \quad (77a)$$

$$\mathbf{Q}_2 = \mathbf{Q}_1 + \Delta\mathbf{Q}_1 \quad (77b)$$

Then, it is checked if $\mathbf{Q}_2$ satisfies $\mathbf{R}(\mathbf{Q}_2) = 0$. If not, the procedure is repeated so that the residue tends to zero.

The expression of the iteration matrix in Eq. (76) for the generic k-th iteration can be rewritten as reported in Eq. (78), considering that the

Table 4
Summary of the numerical implementation of PFM for fracture in LIBs.

Active material	Particle geometry	Approach	Time integration	Software	Ref.
Si	Nanowire	Hybrid	Newmark	MATLAB	[82]
LMO	Cylindrical	Isotropic	Backward Euler	PETSc	[83]
Si	Spherical	Hybrid	Not specified	MATLAB	[84]
$LiMn_2O_4$	Spherical and cylindrical	Hybrid	Backward Euler method	PARDISO solver and COMSOL	[85]
LMO	Spherical and cylindrical	Anisotropic	Backward Euler	FE library deal.II v8.1	[86]
LMO	Spherical and cylindrical	Hybrid	Backward Euler	libMesh and PETSc	[87]
LMO	2D and 3D from SEM image	Isotropic	Backward Euler	Not specified	[44]
Si	Spherical	Isotropic	Not specified	COMSOL	[88]
LFP	Platelet	Isotropic	Not specified	FEniCs	[89]
Generic	Cylindrical	Anisotropic	Backward Euler	FEAP	[90]

residual $\mathbf{R}$ can be split into two components, namely $R = R_{tk}(\mathbf{Q}) + R_{tc}(\dot{\mathbf{Q}})$ depending on $\mathbf{Q}$ and $\dot{\mathbf{Q}}$ respectively.

$$[\mathbf{S}(\boldsymbol{Q}_k)] = \frac{\partial \mathbf{R_{tk}}}{\partial \mathbf{Q}}\bigg|_{\mathbf{Q}_k} + \frac{\partial \mathbf{R_{tc}}}{\partial \mathbf{Q}}\bigg|_{\mathbf{Q}_k} = \frac{\partial \mathbf{R_{tk}}}{\partial \mathbf{Q}}\bigg|_{\mathbf{Q}_k} + \frac{\partial \mathbf{R_{tc}}}{\partial \dot{\mathbf{Q}}}\bigg|_{\mathbf{Q}_k} \frac{\partial \dot{\mathbf{Q}}}{\partial \mathbf{Q}} \tag{78}$$

Where $\frac{\partial \dot{\mathbf{Q}}}{\partial \mathbf{Q}} = \tau$ is a coefficient depending on the integration scheme, which is equal to $\tau = \frac{\gamma}{\beta \Delta t}$ for the Newmark integration scheme, Δt is the time integration step, β and γ are constant parameters, usually set equal to $\beta = \gamma = 0.5$. Finally $[\mathbf{S}(\boldsymbol{Q}_k)]$ in Eq. (78) is written in matrix form according to Eq. (79).

$$[\mathbf{S}(\boldsymbol{Q}_k)] = [\mathbf{K}(\boldsymbol{Q}_k)] + [\mathbf{C}(\boldsymbol{Q}_k)]\tau \tag{79}$$

Where $[\mathbf{K}(\boldsymbol{Q}_k)]$ and $[\mathbf{C}(\boldsymbol{Q}_k)]$ are the tangent stiffness and damping matrices, whose expressions are given in Appendix A.1.

The flowchart reported in Fig. 3d summarizes the procedure to compute the solution of the system of Eqs. (74). At the i-th time step, an initial guess solution $\boldsymbol{Q}^{\boldsymbol{i}}$ is made on the basis of the solution $\boldsymbol{Q}^{\boldsymbol{i-1}}$ obtained from the Newton-Raphson iteration of the previous time step, according to the chosen time integration scheme. Then the residual is computed and the convergence is checked. If the residual is greater than the tolerance, the solution is corrected according to Eq. (77), namely the increment $\Delta \boldsymbol{Q}_1$ is added to the previous solution $\boldsymbol{Q}^i_1$, to get a new solution $\boldsymbol{Q}^i_2$. Then, a new residual is computed with the new solution $\boldsymbol{Q}^i_2$ and so on. When the residual is beneath the chosen tolerance, the solution $\boldsymbol{Q}^i_k$ is the solution of that time step, then the time is incremented and a new guess solution of the following time step $\boldsymbol{Q}^{\boldsymbol{i+1}}$ is made on the basis of $\boldsymbol{Q}^i_k$, and so on.

In the literature, several works adopting the PFM approach to simulate fracture in LIBs were proposed. A brief summary of the numerical implementation of the PFM solving fracture in LIBs is given in Table 4. Both isotropic, anisotropic and hybrid formulations are used, and different time integration methods are adopted. Moreover, different commercial software is employed, namely MATLAB, COMSOL, ABAQUS, FeniCs, FEAP.

4.5. Concluding remarks

- **FEM.** Pro: All the models presented in Section 3 can be solved with FEM. It is an established method, and fracture mechanics is already implemented in most of the FE commercial software. Cons: Crack growth simulation requires updating the geometry of the crack and the mesh according to the crack path, which significantly increases the computation time and the code complexity.
- **XFEM.** Pro: This method does not require the re-mesh stage, which is complex and time-consuming, thus it overcomes the issues hindering the use of FEM for crack growth. Enriched elements are inserted along the supposed crack path. Cons: Few commercial software supports XFEM, and sometimes does not allow multiphysics modeling.
- **Phase-field.** Pro: Crack growth is simulated without the need for a pre-existent crack. The geometric discontinuity is eliminated by using the PF variable and singular elements are not needed. Complex and unknown crack paths can be simulated as the re-meshing is not necessary. Cons: Few commercial software have the phase-field model already implemented.

5. Results of fracture mechanics applied to LIBs

5.1. Phenomena linked to fracture - Fracture relaxation and Li-embrittlement

Mechanics and transport fields influence each other. In particular, lithium is driven by stress from compressive to tensile areas. Then, lithium ions are driven to the crack tip, because it is subjected to significantly higher tensile stress, according to the SIF definition given in Section 3.1.1, with respect to the neighboring areas. The increase in lithium concentration at the crack tip causes an increase in the chemical term of deformation reported in Eqs. (1)a. Assuming that the total deformation is constant, the elastic component of deformation (the first term of Eqs. (1)a) decreases, causing the stress relaxation effect [91].

Some authors measured the fracture toughness of different active materials and noted that it is dependent on the concentration of lithium ions. In particular, high concentration causes an increase in fracture toughness in NMC, LCO, and silicon [92–94]; on the other hand, high lithium concentration causes a decrease in fracture toughness in carbon nanotube because of the reduction of C–C bonds, then it may be assumed that graphite has the same behavior [74,95].

5.2. Static loading — single (de)lithiation

Most of the works in the literature dealt with crack growth in active material particles of LIBs due to single (de)lithiation, thus neglecting fatigue effects. The numerical models were implemented according to Section 4 and fracture mechanics failure criteria reported in Section 3.1.4 were employed.

Active material particles were modeled as spherical or platelet-like bodies, and the cracks were supposed to open according to mode I in most of the works. Thus, the tensile hoop stress induced by lithium diffusion or by the lattice mismatch between phases with different lithium concentrations is the driving force for crack propagation. However, some works dealt with the mixed-mode case as well. Earlier works neglected the mechanical–diffusive coupling, which has been taken into account in the most recent works.

The literature concerning fracture mechanical modeling in LIBs can be grouped according to the three main objectives:

- Study of the factors influencing fracture, including charge/discharge current rate, size and shape of the active material particles, and initial crack length.
- Study of the crack growth stability.
- Study of the crack propagation path.

The main features and results of these numerical models will be explained in the following sections.

Table 5
Summary of the main works existing in the literature dealing with the influence of the operating conditions and geometric properties on fracture in LIBs due to single (de)lithiation.

Particle geometry	Electrode Material	Mode	Driving force	Numerical implementation	Addressed topic	Ref.
Platelet and equiaxed	LFP	I	Stress due to phase transition	G computation with FEM in ABAQUS	Determination of the critical size and current rate for crack growth	[96]
Equiaxed	LCO	I	Diffusion induced stress	G computation with FEM in ABAQUS	Determination of the critical size for crack growth	[97]
Platelet	LFP	I and II	Stress due to phase transition	G computation with FEM in ANSYS	Fracture evaluation under mixed-modes	[98]
Spherical and Ellipsoidal	LMO	I	Diffusion induced stress	XFEM in ABAQUS	Fracture map	[79]
Spherical	LMO	I	Diffusion induced stress	Analytical computation of K_I	Fracture map	[59]
Spherical	LFP	I	Stress due to phase transition	Analytical computation of K_I	Fracture map	[62]
Spherical	LMO	I	Diffusion induced stress	K_I computation with FEM in ANSYS	Evaluation of the effects of geometric factor and current rates on fracture	[11]

5.2.1. Influence of the operating condition and geometric factors

The fracture behavior of active materials is affected by the operating conditions, such as charge/discharge current rate, as well as by geometric factors, such as the size and shape of active material particles and the initial length of micro-flaws. Indeed, these factors influence the stress level within active material particles and the fracture behavior in turn.

The main works dealing with the influence of the operating conditions and geometric properties on fracture are summarized in Table 5.

Different active materials were modeled, such as LFP [62,96,98], LCO [97] and LMO [11,59,79]. Thus, two driving forces for crack propagation were considered according to the type of active material: the stress caused by phase transformation and the diffusion induced stress due to the lithium concentration gradient. For example, crack growth in LFP particles is mainly caused by the transition from Li-poor to the Li-rich phase occurring during (de)lithiation, which generates mismatch strains and stresses at the phase boundary. On the other hand, cracks in LMO and LCO particles propagate due to the stress induced by the lithium concentration gradient.

Pre-existent cracks were considered in all the models and they were placed where the stress driving the crack propagation is maximum. Cracks in LFP particles are inserted both in the *ac* and *bc* planes of the crystal structure, which is the phase boundary orientation [17], whereas superficial or central cracks were considered in LMO and LCO particles.

The mechanical–diffusive coupling explained in Section 2 was often neglected. Thus, the lithium transport equation was solved separately from the fracture computation. Then, the diffusion induced stress was obtained by replacing the lithium concentration with an equivalent temperature distribution, according to the thermal analogy [11,97,98]. The transport equation was not solved in some works, and the mismatch strains derived from the experimental measurements of the crystalline lattice parameters of Li-rich and Li-poor phases were applied as thermal strains [96].

Finally, fracture parameters were computed as the stress distribution is got. Most of the models were implemented with FEM, which is a convenient tool as long as crack propagation is not considered and re-meshing is not needed. Few works used XFEM and others used the analytical approach.

The critical size of active material particles and the current rate which cause crack growth were determined by computing the energy release rate [96,97,99] or the SIF [11] from the J-integral, according to Section 3. The main conclusion achieved in all works was that smaller particles with smaller initial crack lengths and (de)lithiated at lower current rates are less detrimental from the fracture point of view.

Fracture maps provide an effective visualization of fracture-safe and fracture-likely conditions according to geometric factors and current rates. Fig. 4 shows the fracture maps determined by Zhu et al. [79], Woodford et al. [59] and Chen et al. [62], considering spherical and elliptical LMO particles with central crack during discharge, spherical LMO particle with superficial crack during charge and LFP particle with a crack at phase boundary interface during charge, respectively.

The fracture map obtained by Zhu et al. [79] reported in Fig. 4a shows that spherical particles with bigger radius and lithiated at higher current density are more detrimental from the fracture mechanics point of view. A similar trend was also obtained by Woodford et al. [59] and Chen et al. [62], showing that fracture is more likely to occur in bigger particles and at higher current rates, according to Fig. 4c and d. Furthermore, the fracture is triggered based on the fracture toughness value, which is often difficult to measure.

Zhu et al. [79] studied the influence of the particle shape on fracture and their results, reported in Fig. 4b, are consistent with the stress trend reported by Clerici et al. [8], highlighting that the axis ratio ranging between 1 and 2 amplifies the stress, and then the SIF, with respect to the spherical case.

These fracture maps can provide only an approximated estimation of factors leading to crack propagation during charge/discharge because the full coupling between mechanical, lithium diffusion, and fracture was neglected. This means that the reduction of the crack driving force due to lithium accumulation at the crack tip was not modeled, thus the occurrence of fracture was overestimated. Furthermore, the accuracy of the fracture maps can be improved using experimental values of the critical energy release rate G_{cr} and fracture toughness $K_{i,cr}$. Indeed, all the works mentioned above guessed these material properties, as performing experimental measurements is challenging and only a few studies measured critical fracture parameters with nanoindentation [92,101–104].

5.2.2. Stability of the crack growth

The crack growth is unstable when its length increases without increasing the load, leading to rapid failure. Then, it is essential to find the combination of factors that avoid unstable crack growth to prevent rapid LIBs degradation.

The occurrence of stable or unstable crack growth in active materials during charge and discharge can be determined according to the following approaches:

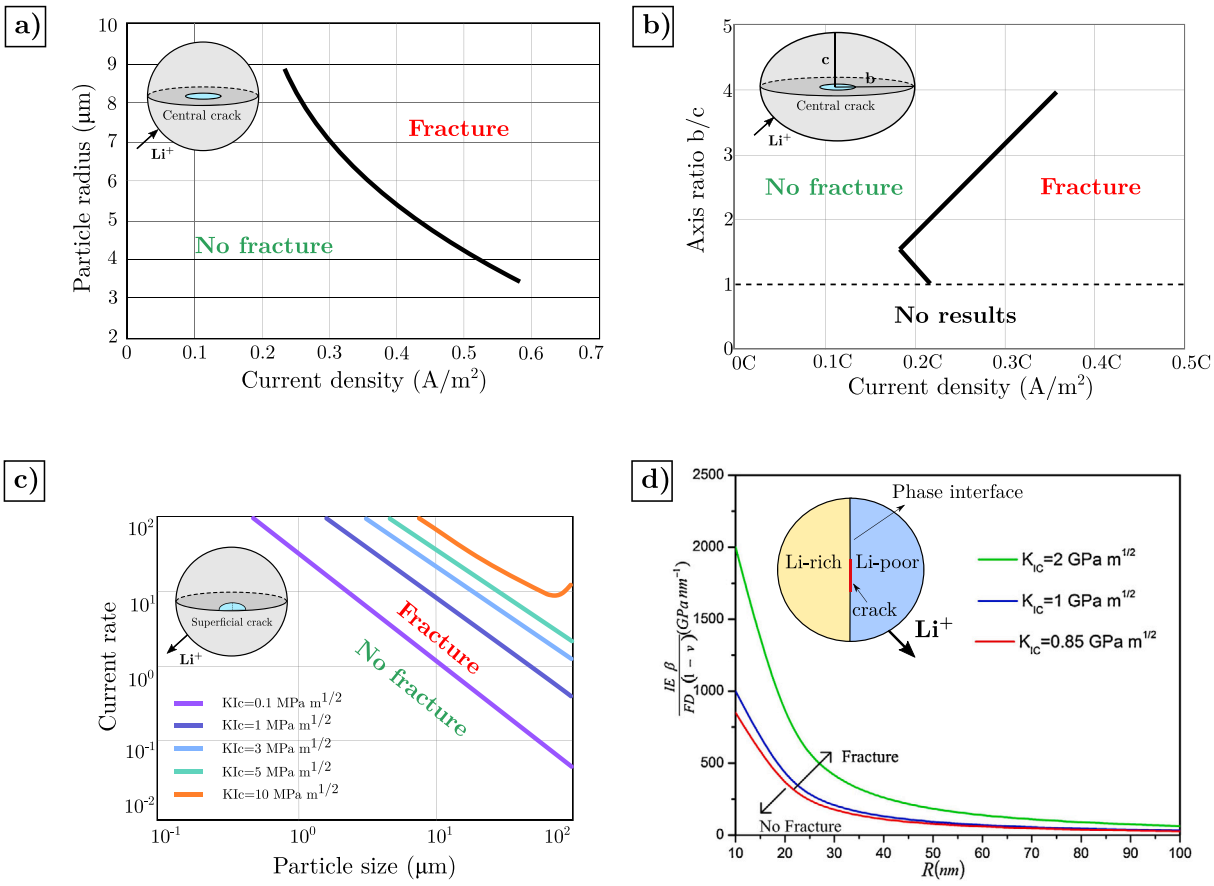

Fig. 4. Fracture map based on the results of [79]: (a) Spherical LMO particle with central crack during discharge and (b) Elliptical LMO particle with central crack during discharge. (c) Fracture map based on the results of [59]: LMO particle with superficial crack during charge. (d) LFP particle with crack at phase boundary interface during charge, where $\frac{IE\beta}{FD(1-\nu)}$ is proportional to the current density. Reprinted with permission from [62].

- Comparison between the crack driving force curve and the resistance curve (R-curve). The crack driving force curve can be expressed as the energy release rate (G) or SIF (K) variation with respect to the crack extension ($\partial G/\partial a$ or $\partial K/\partial a$). Similarly, the R-curve is the critical energy release rate G_{cr} or fracture toughness K_{cr} variation with respect to the crack extension ($\partial G_{cr}/\partial a$ or $\partial K_{cr}/\partial a$) [31]. Crack grows unstably when: $G \geq G_{cr}$ and $\partial G/\partial a \geq \partial G_{cr}/\partial a$ (or $K \geq K_{cr}$ and $\partial K/\partial a \geq \partial K_{cr}/\partial a$).
  In the mechanical field, the SIF is proportional to the crack length and G_{cr} (or K_{cr}) is constant, as represented in Figure S4a. Thus, the crack propagates unstably once that $G \geq G_{cr}$ (or $K \geq K_{cr}$) because the crack driving force curve is always higher than the R-curve, which is 0. On the other hand, the crack driving force curve and the R-curve may have different behavior when both mechanical and diffusive phenomena are present, as shown by Woodford et al. [59] and Xu et al. [74] and represented in Figure S4b. Namely, G (or K) are not directly proportional to the crack length (a) and G_{cr} (or K_{cr}) can depend on a.
- Monitoring the crack length variation over time. Unstable crack growth occurs when crack length suddenly increases. This approach was adopted by Zhang et al. [80], Klinsmann et al. [86, 100] and Mesgarnejad et al. [87].

It was demonstrated that the crack growth stability in active material depends on geometric factors, such as particle size and initial crack length, as well as operating conditions, such as current rate, as these factors influence the driving force for crack growth.

Woodford et al. [59] analyzed the influence of the initial crack length on the crack growth stability (Fig. 5a-b). K_I was computed as a function of the crack length, considering a superficial crack in LMO spherical particle during delithiation. They concluded that smaller cracks are more detrimental since they undergo unstable crack growth, resulting in an increase in the K_I as the crack length increases. Then, the crack can extend by a noticeable distance, and the crack tip can overcome the compressive regions which would cause the crack to arrest, leading to rapid breakage occur. On the other hand, larger cracks grow stably until arresting when $K_I = K_{I,cr}$, as shown in Fig. 5b. This is because the tensile hoop stress decreases and becomes compressive, going from the particle surface to the center. Thus, larger cracks experience lower stresses than smaller cracks, as the crack tip of larger cracks is deeper and away from the surface.

Klinsmann et al. [100] modeled axisymmetric LMO cylindrical particles with a superficial crack during delithiation. Referring to Fig. 5c, they showed that the crack does not grow if the initial length is shorter than a critical threshold a_c, then it becomes suddenly unstable as soon as the initial crack length is slightly higher than a_c. On the other hand, the crack growth becomes stable when the initial length is larger than a threshold value ($a > a_s$), which depends on the geometry and operating conditions.

In general, stable propagation follows unstable propagation, depending on the combination of initial crack growth, current rate, and particle radius. Klinsmann et al. [100] demonstrated the existence of a minimum C-rate (C_{min}) below which crack propagation does not occur, depending on the particle radius and initial crack length. As the C-rate increases above C_{min}, the critical threshold a_c triggering unstable crack growth decreases because of the higher stress. The threshold value for the stable crack growth a_s decreases as well, then, the unstable crack growth regime is shorter at higher C-rate. Finally,

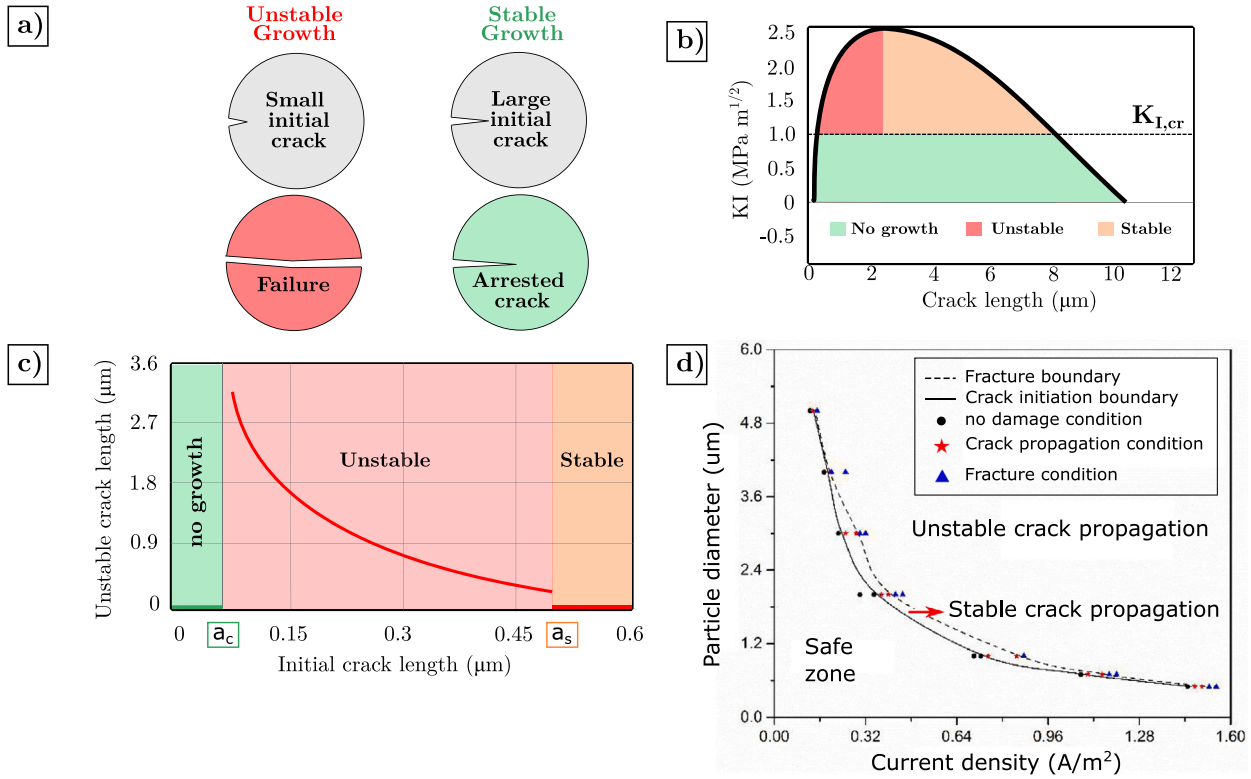

Fig. 5. Crack propagation stability. (a) Schematic representation of crack growth stability based on the initial crack length. (b) K_I as a function of the crack length. The particle radius is 21 μm and C-rate is 5 [59]. (c) Crack length increment during unstable crack growth as a function of the initial crack length a. The particle radius is $r = 5$ μm and the C-rate is 5 [100]. (d) Fracture map as a function of particle diameter and current density. Reprinted with permission from [81].

Klinsmann et al. [100] determined the critical particle radius leading to crack growth with fixed initial crack length and C-rate. a_c, C_{min} and a_s decrease in particles with a larger radius, thus only stable crack growth can occur in larger particles at a higher C-rate or with a longer initial crack. However, the results of Klinsmann et al. [100] for lithium extraction do not agree with other results in the literature.

On the other hand, Klinsmann et al. [86] explained that during lithium insertion unstable crack growth occurs in larger particles and at higher current rate. Smaller crack length leads to unstable crack growth, as during extraction. They derived an approximated stability law expressed in Eq. (80).

$$\frac{1}{2}\frac{\sqrt{r}}{\gamma}\frac{1-(a/r)^{\gamma}}{(a/r)^{\gamma-1/2}} \leq 1 \tag{80}$$

Where $\gamma \geq 1$ is the convexity exponent of lithium distribution, proportional to the current rate. Eq. (80) provides the relation between factors influencing the crack propagation stability, although it underestimates the range of crack length undergoing stable propagation.

Zhang et al. [69] recognized three crack growth regimes in LMO cylindrical particles during insertion, namely no crack propagation, stable crack propagation, and stable followed by unstable crack propagation. Furthermore, they showed that unstable crack growth is more likely to occur when the particle radius is larger and at higher C-rates, which is in agreement with Klinsmann et al. [86].

Three crack growth regimes in lithiated silicon nanowires were also recognized by Grantab et al. [91], namely no crack growth, stable crack growth, which means that crack partially grows across the nanowire but it arrests ultimately, and unstable crack growth. The arrest of the crack is attributed to the accumulation of lithium ions at the crack tip, relaxing the stress and the crack driving force. The results show that unstable crack growth is more likely to occur at a higher C-rate and in larger particles, on the other hand, a combination of C-rate and particle radius which does not lead to complete particle failure exists. Finally, a lower C-rate or smaller particle radius can prevent crack growth.

Zhu et al. [81] studied the initiation and propagation of cracks in NMC particles during lithium extraction, varying the current density and particle size. Differently from the works discussed above, no pre-existent cracks were assumed in the model. Three cracking stages were recognized, based on the combination of current density and particle size: (a) the safe region, where the stress is not high enough to induce crack initiation, (b) the stable crack propagation region, and (c) the unstable crack propagation region, which rapidly leads to particle failure. The combination of particle size and current density giving rise to the three cracking stages is reported in Fig. 5d.

5.2.3. Crack propagation path

Several works dealt with the prediction of the crack propagation path during (de)lithiation. A summary of the main works existing in literature is provided in Table 6. The fracture models and the numerical implementation were generally chosen according to the type of active material and the corresponding fracture mechanism.

Some works modeled the intergranular fracture occurring at the grain boundary of NMC primary particles [69,71,72,74,81]. Zhang et al. [69] modeled crack nucleation and initiation along NMC primary particles during charge/discharge. It was found that the crack initiates at the particle center, then it grows toward the particle surface and branches in two directions, with additional minor cracks appearing near the two initial branches of the main crack, as shown in Fig. 6a. This behavior is consistent with experimental studies [106].

Tian et al. [71,72] employed the model developed in [69] to analyze the effects of fracture toughness and C-rate on the intergranular cracking in NMC particles during lithiation. The results show that the fracture toughness and C-rate variation modify the crack propagation pattern and crack distribution as well, as depicted in Fig. 6b.

Table 6
Summary of the main models in the literature describing the crack propagation path in different electrode active materials during single charge/discharge cycle.

Electrode material	Fracture mechanism	Fracture model	Implementation	Software	Ref.
NMC	Intergranular cracking	CZM	FEM	ABAQUS	[69]
NMC	Intergranular cracking	CZM	FEM	ABAQUS	[72]
NMC	Intergranular cracking	CZM	FEM	ABAQUS	[71]
NMC	Intergranular cracking	CZM	FEM	COMSOL	[105]
NMC	Fracture during lithiation/delithiation	CZM	XFEM	ABAQUS	[81]
LMO	Fracture during lithiation	FEM	PFM	Not specified	[44]
LFP	Phase transformation and fracture	FEM	PFM	Not specified	[89]
Silicon	Fracture during lithiation	FEM	PFM	COMSOL	[88]

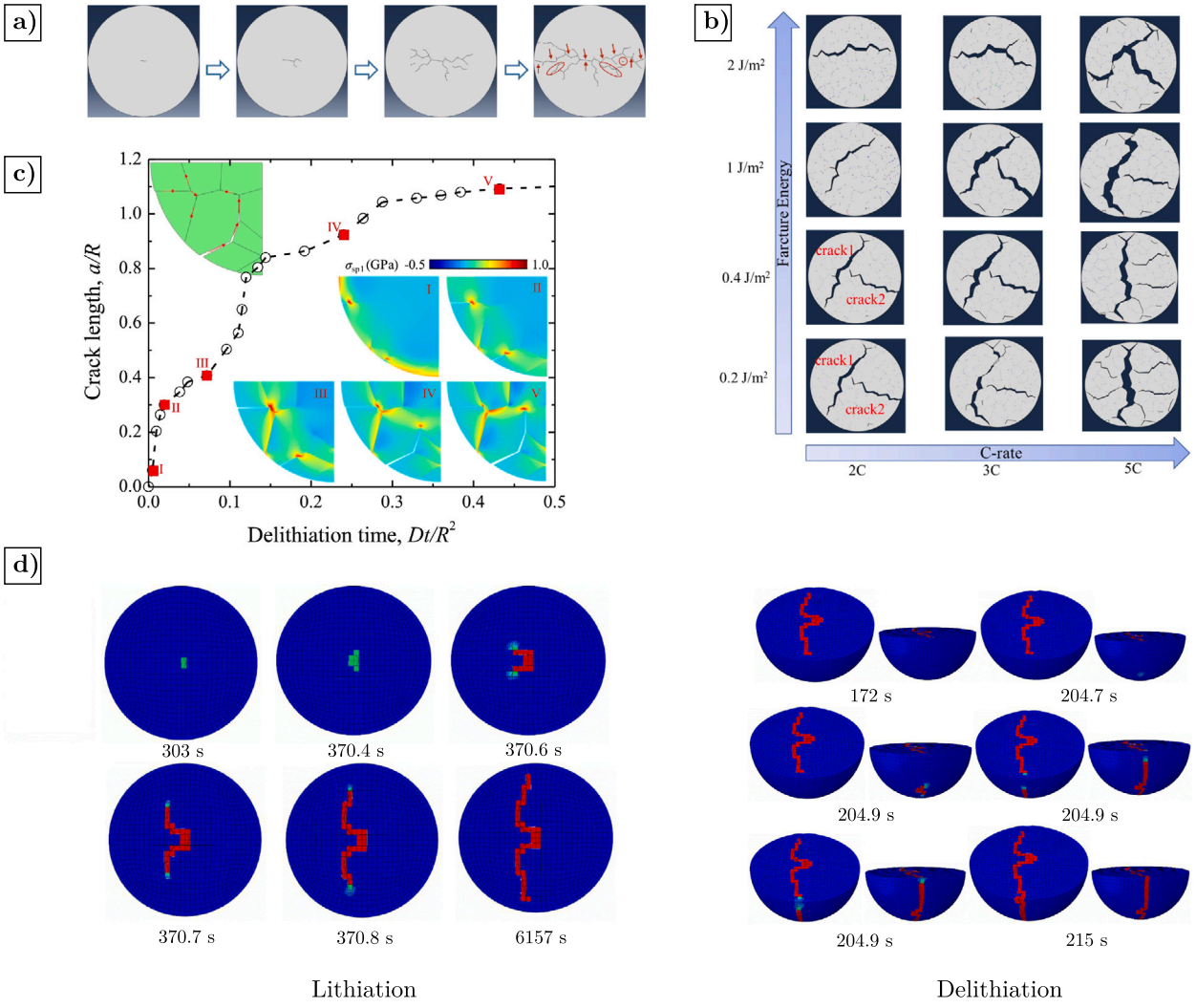

Fig. 6. (a) Crack evolution in NMC particle during charge/discharge. Reprinted with permission from [69]. (b) Crack evolution in NMC particle during charge/discharge as a function of the C-rate and fracture energy. Reprinted with permission from [72]. (c) Crack evolution in NMC particle during delithiation. The insets in the plot represent the principal stress at various delithiation times and the corresponding crack morphologies indicated by the red arrows. Reprinted with permission from [74]. (d) Crack initiation and propagation in single-crystal NMC particle due to lithiation and delithiation with a current density of 0.37 A/m^2. Reprinted with permission from [81]. Crack evolution in LMO particle during potentiostatic charge. The cracked elements are represented in red in the Figure. (For interpretation of the references to color in this figure legend, the reader is referred to the web version of this article.)

Xu et al. [74] modeled intergranular cracking in NMC during delithiation. Based on the experimental measures reported in [92], fracture toughness dependent on lithium concentration was considered in the model. The lower the lithium ion concentration, the lower the fracture toughness and the more likely the crack propagation. Xu et al. [74] showed that during delithiation cracks form first on the particle surface due to the higher stress, consistent with DIS calculation [7]. At the beginning of delithiation, the crack grows fast due to the rapid decrease in the fracture toughness caused by the lower lithium concentration, as shown in Fig. 6c. As the delithiation proceeds, several cracks are triggered in the particle due to the drop in the fracture toughness. Furthermore, as the crack proceeds toward the particle center, the tip encounters higher lithium concentration and the fracture toughness is higher, whereas the tensile stress driving the crack growth decreases or becomes compressive. As a result, the crack grows less quickly, until it arrests.

Finally, Zhu et al. [81] studied the crack evolution in NMC single-crystal spherical particles without pre-existent cracks during lithiation–delithiation, as reported in Fig. 6d. It is shown that the crack initiates and grows where the tensile stress is maximum, i.e. at the core of the particle during the lithiation phase and on the particle surface in the following delithiation, consistent with DIS computation [7]. The results show that the surface and internal cracks grow and merge ultimately at the end of delithiation, leading to the complete fracture of the particle.

Miehe et al. [44] modeled the crack propagation during potentiostatic charge in LMO particles without assuming pre-existent cracks, considering a 2D geometry in plane strain conditions and a 3D geometry with an irregular shape. The crack pattern in the 2D model is quite smooth, several cracks initiate and propagate in the particle, but no crack branching is recognized, as shown in Figure S5a. On the contrary, complex 3D crack surfaces appear in the 3D model, as shown in Figure S5b.

O'Connor et al. [89] examined the phase transformation and fracture arising in LFP particles with plate-like shapes during charge/discharge. The crack propagation path follows the regions of high stress, which are located at the phase boundary interface, and crack kinking and branching occur according to the phase boundary interface evolution. This mutual interaction between the crack path and the phase boundary evolution was also confirmed by experimental studies [107].

Finally, Liu et al. [88] employed the PFM to describe the crack evolution within silicon nanoparticles during lithiation. Their results are quite in agreement with the experimental TEM images, as shown in Figure S5c.

5.3. Cyclic loading

Active material particles are subjected to repeated charge/discharge cycles during battery operation thus experiencing fatigue damage. Although the static numerical models presented in the previous sections are suitable to model fracture due to a single (de)lithiation, they cannot track the crack growth due to cyclic loading.

Paris' law is the most common approach to account for fatigue crack growth in LIBs because of the straightforward implementation. On the other hand, the models in literature based on Paris' law cannot capture complex fracture mechanisms occurring in the active material particles. The main reasons are summarized as follows:

- Stand-alone particles with idealized geometry (spherical) were considered.
- Paris' law was not implemented in a FEM (or XFEM) framework, thus the crack increment was computed analytically using Eq. (37) without modeling the evolution of the crack path.
- The SIF was computed analytically, using the geometric factor of the plates, which is far from the case of active material particles. This allows dealing with crack propagation completely analytically but the accuracy is affected.
- Paris' coefficients were fitted or guessed, without knowing how far the true values are. It would be necessary to obtain such parameters experimentally.
- Paris' law can predict crack growth in the stable region. It is unsuitable to model crack nucleation and unstable crack growth.

Few works modeled fracture in LIBs caused by repeated charge/discharge cycles [74,85,108]. Boyce et al. [108] and Ai et al. [85] adopted the PFM, on the other hand, CZM implemented in a FEM framework was employed by Xu et al. [74].

Boyce et al. [108] predicted fracture occurring in the active material particles of NMC622 by combining the advanced X-ray computed tomography imaging with a coupled electro-chemo-mechanical model and PFM. This approach gives a realistic prediction of fracture as it allows considering the electrochemistry of the whole LIB, the mechanical–diffusive coupling, as well as overcoming the hypothesis of the stand-alone active material particles with idealized geometry.

Boyce et al. [108] showed that the occurrence of fractures depends on:

- Particle location across the electrode thickness. The fractures occur more often in particles near the separator rather than near the current collector. This is mainly caused by diffusion-limited transport, which leads to inhomogeneous lithium ions distribution throughout the electrode, especially at higher current rates, influencing the mechanical stress distribution and fracture ultimately. Particles near the separator are subjected to a greater lithium flux, leading to a greater concentration gradient, stress, and fracture ultimately.
- Electrode thickness. Fracture is distributed more uniformly throughout the electrode microstructure when the electrode is thinner, on the other hand, fracture appears concentrated especially near the separator in thicker electrodes.
- Particle size. Larger particles experience larger tensile stresses than smaller particles, affecting their fracture behavior.
- Current rate. A higher current rate increases the concentration gradient within the active material particles, leading to higher mechanical stress.
- Electrochemical cycling. Most of the damage occurs during the first cycle and larger voltage ranges increase cracking, as shown in Fig. 7a.

The model developed by Boyce et al. [108] gives practical suggestions and defines the operating conditions which can limit mechanical degradation and performance decay. Despite this, some points are still lacking in the model, such as considering only void-driven fracture and neglecting both the intergranular and intragranular cracking, although several experimental observations demonstrated that these fracture mechanisms typically occur in NMC [17,106]. Furthermore, few charge/discharge cycles were simulated, with respect to the LIB life cycle.

Xu et al. [74] modeled the intergranular cracking in NMC due to repeated charge/discharge cycles, considering that fracture toughness decreases with increasing the number of cycles, according to experimental measures reported in [92] and resumed in Fig. 7c. On the other hand, fracture toughness is considered constant during one cycle. Xu et al. [74] showed that the crack evolution has a "grow-stagnate-grow" behavior, as evidenced in Fig. 7d, which reports the crack length increment as a function of the number of cycles. The crack starts to grow when the decrease in the fracture toughness is enough to trigger the crack propagation. Then, the crack growth is slowed down because of crack kinking at the joints of the grain boundaries, and finally the crack growth rate increases again because of the significant decrease in the fracture toughness after a large number of cycles.

The estimated crack growth trend appears quite in agreement with the recent in-situ SEM experimental measurements performed by Chen et. [109], who monitored the crack growth in NMC particles during charge/discharge cycles, as shown in Fig. 7e.

Ai et al. [85] accounted for the fatigue crack growth in LMO particles during repeated charge/discharge cycles by combining a mechanical–diffusive model for lithium transport with a PFM for fatigue fracture. Hundreds of charge/discharge cycles were simulated, in contrast with the works mentioned above, which considered a smaller number of cycles. Crack growth in LMO particles with ideal spherical and cylindrical shapes, as well as a realistic ellipsoid with a central pre-existent crack, were simulated. Multiple crack interactions, such as merging, appeared when the particle with realistic geometry was considered, as reported in Fig. 7b. Furthermore, Ai et al. [85] demonstrated that cycling operations are more detrimental from the mechanical degradation point of view, as the critical values of C-rate,

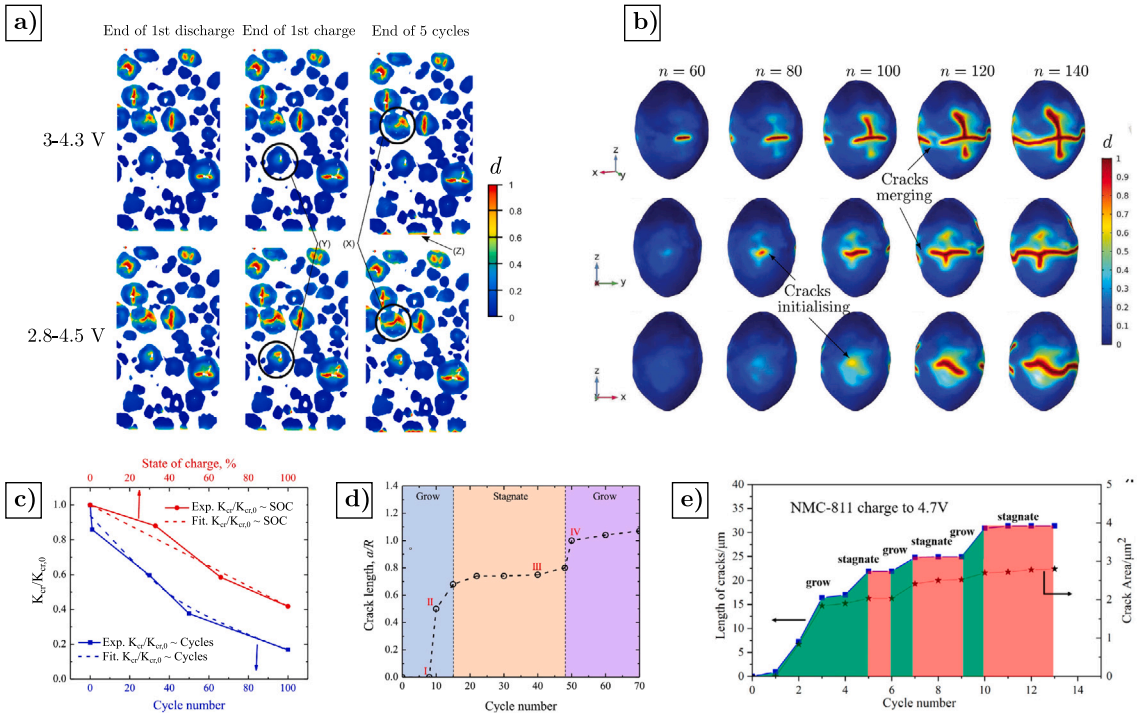

Fig. 7. (a) Fracture evolution in NMC particle cycled over 5 cycles in terms of PF variable, considering two voltage ranges, i.e. 3–4.3 V and 2.8–4.5 V. Reprinted with permission from [108]. (b) Crack evolution in LMO particle with a realistic elliptical shape. Reprinted with permission from [85]. (c) Fracture toughness (K_{cr}) variation with lithium concentration and the number of cycles, where $K_{cr,0}$ is the initial fracture toughness and (d) Intergranular crack increment in NMC particle as a function of the number of cycles. Reprinted with permission from [74]. (e) Experimental measurement of the intergranular crack evolution with in-situ SEM analysis. The increment in crack length and area is plotted as a function of the number of cycles. Reprinted with permission from [109].

particle size and initial crack length to avoid fracture are lower than the ones reported in literature according to the static fracture models.

5.4. Concluding remarks

A fundamental distinction is made on the basis of the applied load: static (single (de)lithiation) and cyclic (a large number of charge/discharge cycles). Although the static load is not representative of real usage of the battery, it is meaningful for the following purposes:

- Creating fracture map, providing the conditions (current rate, particle radius, and fracture toughness) which cause fracture or not. Fracture is triggered with a high current rate and particle radius, and low fracture toughness.
- Predicting the stability of the crack. Contrary to what one might expect, longer cracks ensure stability. This happens because stress is not constant within the particle, and the tip is away from the area subjected to the maximum stress where the crack was nucleated. Most of the works agree that lower current, smaller particle radius, and longer initial crack lead to stability, with few exceptions.
- Predicting the crack path. More complex models aimed to estimate the crack propagation path, even in reconstructed geometries and particles made of aggregated primary grains. It is difficult to find a consistency between the results of the different models, as they significantly depend on the initial assumption and the type of model.

Very few works considered a cyclic load and fatigue fracture, although it well represents the usage of LIBs. Interestingly, Xu et al. [74] modeled the crack growth along the grain boundaries of a NMC particle, founding a good correspondence with experimental measurements [109].

6. Degradation modeling

Many degradation models have been proposed to predict the capacity fade of LIBs caused by electrochemical and mechanical processes. Models can be empirical, machine-learning, or physics-based. The first two can be effective, but the former lacks in generality, as it is applicable just in the same conditions and with the same LIB chemistry used in the tests, and the latter has poor interpretability and requires a large amount of data to be effective. On the other hand, physical-based models mathematically describe the processes causing the capacity fade with PDEs. They are robust and general, but the difficulty in measuring or estimating the physical parameters involved in the equations, and their complexity, are significant limitations.

This section explains the most popular approach to deal with degradation in LIBs, avoiding excessive complexity but guaranteeing good accuracy. The most common processes causing capacity fade are: (a) isolation of active material, (b) solid electrolyte interphase (SEI) growth, (c) surface cracking, (d) active material dissolution, (e) lithium plating. The effects of these processes are just two: the loss of lithium inventory (LLI) and the loss of active material (LAM), both causing capacity fade ultimately.

To be coherent with the topic of the review, just the processes linked to fracture will be covered, namely surface cracking, SEI growth and isolation of active material. The reader is suggested to refer to specific works for more details concerning the other degradation mechanisms [110,111] and their modeling [112,113].

6.1. Loss of lithium inventory (LLI)

The loss of lithium inventory (LLI) is caused by the SEI formation and growth, limited to the degradation processes considered in this work. All the models in the literature considered SEI growth over graphite, as far as the authors know, but side reactions are known

to occur even at the interface between electrolyte and cathode active materials [17,114,115].

SEI is commonly considered to be made of lithium ethylene dicarbonate ($(CH_2OCO_2Li)_2$) that is formed by the reaction between ethylene carbonate (EC), which is a solvent contained in the electrolyte, lithium ions and electrons on the electrode surface, according to the reaction scheme in Eq. (81)a-c [116].

$$EC + e^- \iff EC^- \tag{81a}$$

$$2EC^- + 2Li^+ \iff (CH_2OCO_2Li)_2 + C_2H_4 \tag{81b}$$

$$2S + 2e^- + 2Li^+ \iff SEI \tag{81c}$$

Where S stays for solvent (EC). As a result, two lithium ions are consumed per SEI molecule produced, as resumed in Eq. (81)c.

The formation of the SEI layer occurs predominantly during the first cycles when the electrode surface is exposed to the electrolyte for the first time. Once the SEI layer is formed, it decreases further side reactions, because it acts as a passivation layer that allows the transport of lithium ions only, and prevents direct contact between the electrode and electrolyte. However, the SEI layer is porous and allows the diffusion of some of the solvents contained in the electrolyte. This causes the side reactions to occur during each charge/discharge cycle, thickening the SEI continuously. Anyway, a thicker SEI layer hinders the diffusion of the electrolyte components, decreasing the rate of SEI formation. As a result, a high rate of SEI growth occurs during the first cycles, which progressively decreases as a function of time. The same trend is experimentally observed on the capacity fade, which usually, but not always, has a trend proportional to $t^{0.5}$ at low current rates or when no current is applied (the so-called calendar aging) [113,117–120]. When cycling at higher current rates, steeper capacity fade occurs, suggesting that other mechanisms occur, accelerating the SEI growth and causing LAM potentially. Further details concerning the SEI formation, morphology, features, and characterization, can be found in the comprehensive review by An et al. [121].

It has been shown that cracks propagate because of battery operation in Section 5, as well as observed in [17], making new active material surfaces exposed to the electrolyte, where further SEI decomposition can occur. As a consequence, capacity fade due to SEI precipitation can be split into three contributions:

1. SEI growth on the nominal electrode surface (calendar aging).
2. SEI formation on the new surfaces created by cracks.
3. SEI growth on the new surfaces created by cracks.

1) Generally speaking, the formation of SEI can occur following two mechanisms: the reaction is controlled by kinetics and by the diffusion of the solvent through the porous SEI layer. In the former case, the solvent diffusion is extremely fast; in the latter, the reaction kinetic is much faster than the diffusion. In some cases, both the reaction kinetics and solvent diffusion can matter in a similar magnitude.

Then, the SEI growth on the surfaces of active material particles, which is independent of fractures, has been commonly modeled in the literature according to three approaches: (a) kinetic-limited [113,122,123], (b) solvent diffusion-limited [112,113,124] and (c) more general mixed-mode models considering both kinetic and diffusion [113,116,125–129].

The SEI growth rate ($\frac{dL_{SEI}}{dt}$) is a function of the current density of the SEI side reaction (i_{SEI}), according to Eq. (82).

$$\frac{dL_{SEI}}{dt} = \frac{V_{SEI}}{n_{SEI}F} i_{SEI} \tag{82}$$

Where $V_{SEI} = \frac{M_{SEI}}{\rho_{SEI}}$ is the SEI molar volume, M_{SEI} and ρ_{SEI} are the molar mass and the density of the SEI, n_{SEI} is the ratio between the moles of lithium ions consumed and SEI produced and F is the Faraday's constant.

In the more general mixed-mode model, the SEI growth rate is controlled both by the reaction kinetics on the surface of the particles (Eq. (83)) and the diffusion of the solvent, which follows the mass conservation law (Eq. (84)).

$$i_{SEI} = -FK_{SEI} c_{solv}^{electrolyte} \exp\left(-\frac{\beta F}{RT}\eta_{SEI}\right) \tag{83a}$$

$$\eta_{SEI} = U - \eta - \frac{L_{SEI}}{K_{SEI}} i \tag{83b}$$

$$\begin{cases} \dfrac{\partial c_{solv}}{\partial t} - D_{solv}\dfrac{\partial^2 c_{solv}}{\partial r^2} + \dfrac{dL_{SEI}}{dt}\dfrac{\partial c_{solv}}{\partial r} = 0 \\ -D_{solv}\dfrac{\partial c_{solv}}{\partial r}\Big|_{r=R} + \dfrac{dL_{SEI}}{dt} c_{solv}^{AM} = \dfrac{i_{SEI}}{F} \\ c_{solv}|_{r=R+L_{SEI}} = c_{solv}^{electrolyte} \end{cases} \tag{84}$$

Where K_{SEI} is the reaction rate constant, c_{solv}, c_{solv}^{AM} and $c_{solv}^{electrolyte}$ are the solvent concentration in the SEI layer, on the active material particles surface and in the electrolyte, respectively (Figure S6). β is the transfer coefficient, η_{SEI} is the overpotential of the side reaction, U and η are the OCV and the overpotential of the electrode respectively, i is the total current density, L_{SEI} is the thickness of the SEI layer and D_{solv} is the diffusion coefficient of the solvent in the SEI layer.

Some authors [124,126] assumed a linear diffusion across the SEI layer and a constant solvent concentration in the electrolyte (Figure S6), thus the term $\frac{\delta c_{solv}}{\delta r}$ is linearized, and the flux of the solvent at the SEI/electrolyte interface reported in the second of Eq. (84) is rewritten according to Eq. (85).

$$-D_{solv}\frac{\Delta c_{solv}}{L_{SEI}} + \frac{dL_{SEI}}{dt} c_{solv}^{AM} = \frac{i_{SEI}}{F} \tag{85}$$

Where $\Delta c_{solv} = c_{solv}^{electrolyte} - c_{solv}^{AM}$. Finally, the SEI thickness growth rate ($\frac{dL_{SEI}}{dt}$) is expressed according to Eq. (86) combining Eqs. (82), (83), (85) and considering that $c_{solv}^{electrolyte} = \Delta c_{solv} + c_{solv}^{AM}$. Eq. (86) considers the diffusion and kinetic driving forces equally significant in the growth of the SEI layer.

$$\frac{dL_{SEI}}{dt} = \frac{V_{SEI} c_{solv}^{electrolyte}}{\left[K_{SEI}\exp\left(-\frac{\beta F}{RT}\eta_{SEI}\right)\right]^{-1} + \left[\frac{D_{solv}}{\left(1-\frac{M_{SEI}}{\rho_{SEI}} c_{solv}^{AM}\right)L_{SEI}}\right]^{-1}} \tag{86}$$

The term $\left(1 - \frac{M_{SEI}}{\rho_{SEI}} c_{solv}^{AM}\right)$, which comes from the convective term caused by the growth of the SEI layer thickness ($\frac{dL_{SEI}}{dt} c_{solv}^{AM}$) in the mass conservation law (Eq. (84)), is often considered as negligible. In this case, Eq. (86) has the same form as the one reported in [113,127].

The term $K_k = \left[K_{SEI}\exp\left(-\frac{\beta F}{RT}\eta_{SEI}\right)\right]^{-1}$ at the denominator of Eq. (86) takes into account for the reaction kinetics, on the other hand, the term $K_d = \left[\frac{D_{solv}}{\left(1-\frac{M_{SEI}}{\rho_{SEI}} c_{solv}^{AM}\right)L_{SEI}}\right]^{-1}$ considers the solvent diffusion. Thus, the general mixed-mode model of the SEI growth reaction in Eq. (86) can be further simplified according to Eq. (87) if one mechanism is predominant with respect to the other.

$$\frac{dL_{SEI}}{dt} = \begin{cases} V_{SEI} c_{solv}^{electrolyte} K_{SEI}\exp\left(-\frac{\beta F}{RT}\eta_{SEI}\right) & \text{Kinetic-limited: } K_d \ll K_k \\ V_{SEI} c_{solv}^{electrolyte} \frac{D_{solv}}{\left(1-\frac{M_{SEI}}{\rho_{SEI}} c_{solv}^{AM}\right)L_{SEI}} & \text{Diffusion-limited: } K_k \ll K_d \end{cases} \tag{87}$$

In general, the SEI thickness is obtained by integrating Eq. (86), as reported in Eq. (88) [127].

$$L_{SEI}(t) = \frac{-1+\sqrt{1+At}}{B} \tag{88a}$$

$$A = \frac{2V_{SEI}c_{solv}^{electrolyte}\left(1-\frac{M_{SEI}}{\rho_{SEI}}c_{solv}^{AM}\right)}{D_{solv}}K_{SEI}^2\left[\exp\left(-\frac{\beta F}{RT}\eta_{SEI}\right)\right]^2 \tag{88b}$$

$$B = \frac{\left(1-\frac{M_{SEI}}{\rho_{SEI}}c_{solv}^{AM}\right)}{D_{solv}}K_{SEI}\exp\left(-\frac{\beta F}{RT}\eta_{SEI}\right) \tag{88c}$$

In the extreme cases of kinetic or diffusion-limited process, Eq. (87) can be directly integrated instead of Eq. (86). In those cases, the SEI thickness is expressed according to Eq. (89).

$$L_{SEI}(t) = \begin{cases} \left[V_{SEI}c_{solv}^{electrolyte}K_{SEI}\exp\left(-\frac{\beta F}{RT}\right)\right]\cdot t & \text{Kinetic-limited: } K_d \ll K_k \\ \sqrt{\left[\frac{V_{SEI}c_{solv}^{electrolyte}D_{solv}}{\left(1-\frac{M_{SEI}}{\rho_{SEI}}c_{solv}^{AM}\right)}\right]}\cdot\sqrt{t} & \text{Diffusion-limited } K_k \ll K_d \end{cases} \tag{89}$$

At the first cycles, the SEI layer is thin, then the kinetic contribution prevails on the diffusive one (Eq. (89)). As a result, the SEI layer grows linearly with time ($L_{SEI} \propto t$), as observed by [120]. As the SEI layer increases, the two contributions matter in a similar way, according to Eq. (88). Finally, when the SEI layer is thick, the diffusive contribution prevails because thicker SEI hinders the diffusion of the electrolyte components (Eq. (89)). As a result, the SEI thickness grows with the square root of time ($L_{SEI} \propto \sqrt{t}$), as observed by [119].

Finally, the rate of capacity fade caused by calendar aging is computed according to Eq. (91). The increase of SEI thickness with time $\left(\frac{dL_{SEI}}{dt}\right)$ is replaced by $\frac{dL_{SEI}}{dN}$ according to Eq. (90) to compare the SEI growth rate due to calendar aging to other sources of damage proportional to the number of cycles.

$$\frac{dL_{SEI}}{dN} = \frac{dL_{SEI}}{dt}t_N \tag{90}$$

Where t_N is the time required for one cycle.

$$\left.\frac{dQ}{dN}\right|_1 = \frac{n_{SEI}F\rho_{SEI}}{M_{SEI}}A_0\frac{dL_{SEI}}{dN} \tag{91}$$

Where $A_0 = 4\pi R^2(1+2\rho_c l_c a_0)$ is the initial particle surface, considering pre-existent cracks with initial length a_0, ρ_c is the crack density, namely the number of cracks per surface unit and l_c is the crack width. Then, $A_0\frac{dL_{SEI}}{dN}$ is the increase in volume of the SEI layer, $A_0\frac{dL_{SEI}}{dN}\rho_{SEI}$ is the increase in mass of the SEI layer and $\frac{A_0\frac{dL_{SEI}}{dN}\rho_{SEI}}{M_{SEI}}$ is the moles increase of the SEI. Then, Eq. (91) tells the amount of charge of lithium ions consumed per unit of SEI layer thickness created.

(2) Cracks make new surfaces of active material available for SEI formation. Then the amount of SEI formation increases as long as cracks grow.

The rate of capacity fade caused by the formation of SEI layer on the cracks surfaces is computed in Eq. (92).

$$\left.\frac{dQ}{dN}\right|_2 = \frac{n_{SEI}F\rho_{SEI}}{M_{SEI}}L_{SEI,0}\frac{dA_c}{dN} \tag{92}$$

Where $L_{SEI,0}$ is the thickness of the SEI layer which is assumed to form instantaneously on the cracks surfaces. $\frac{dA_c}{dN}$ is the increase of the cracks surfaces as a function of the number of charge and discharge cycles, and is computed in Eq. (93)a.

$$\frac{dA_c}{dN} = \frac{dA_c}{da}\frac{da}{dN} \tag{93a}$$

$$A_c = 2a_{sv}\varepsilon_a A_e L_e a\rho_c l_c \tag{93b}$$

$$\frac{da}{dN} = C\Delta K^m = C(\sigma_{\theta,max}b\sqrt{\pi a})^m \tag{93c}$$

Where A_c is the area of a single crack and is computed in Eq. (93)b. a_{sv} is the surface-to-volume ratio of the active material particles ($a_{sv} = 3/R$ assuming a spherical shape). $A_e \cdot L_e$ is the volume of the electrode layer (A_e is the area and L_e is the thickness) and ε_a is the percentage of active material in the electrode volume. a and l_c are the crack length and width, respectively.

The increase of crack length ($\frac{da}{dN}$) is computed in Eq. (93)c according to Paris' law explained earlier in Section 3.1.4. It is highlighted that the geometric factor of an infinite plate is commonly considered ($b\sqrt{\pi}$ with $b = 1.12$), which is a considerable simplification.

(3) Finally, the rate of capacity fade due to SEI growth on the cracks surfaces is considered in Eq. (94). It is computed similarly to the calendar aging reported in Eq. (91), which quantifies the rate of capacity fade due to the SEI growth on the initial particle surface, but the increasing surfaces created by cracks are considered instead of the initial area of the particle surface.

$$\left.\frac{dQ}{dN}\right|_3 = \frac{n_{SEI}F\rho_{SEI}}{M_{SEI}}\sum_{i=1}^{N}\left(\frac{dA_c}{dN}\right)_i\left(\frac{dL_{SEI}}{dN}\right)_{N-i} \tag{94}$$

Where i is the i-th charge/discharge cycle.

The total rate of capacity fade for a single electrode particle is got adding together the three contributions reported in Eqs. (91), (92) and (94), as explained in Eq. (95).

$$\left.\frac{dQ}{dN}\right|_{LLI} = \left.\frac{dQ}{dN}\right|_1 + \left.\frac{dQ}{dN}\right|_2 + \left.\frac{dQ}{dN}\right|_3 \tag{95}$$

Then, the total amount of capacity fade in terms of lithium inventory (LLI) due to the calendar and cycling aging is computed integrating Eq. (95) and dividing by the initial capacity of the single electrode particle after the formation cycle (Q_{init}), as reported in Eq. (96).

$$CF|_{LLI} = \frac{\int_1^N \left.\frac{dQ}{dN}\right|_{LLI}dN}{Q_{init}} = \frac{\int_1^N \left.\frac{dQ}{dN}\right|_{LLI}dN}{q_r Q_e\left(\frac{4}{3}\pi R^3\rho_e\right)} \tag{96}$$

Where q_r is a formation cycle efficiency, which is assumed to be 0.9 [35], Q_e and ρ_e are the specific capacity and density of the electrode active material, respectively.

The dependence of the capacity fade on temperature was considered by some authors considering Arrhenius dependent Paris coefficient (C) and SEI growth rate (K_{SEI}), according to Eqs. (97)a-b.

$$C = C_0 e^{-\frac{E_{a,1}}{RT}} \tag{97a}$$

$$K_{SEI} = K_{SEI,0}e^{-\frac{E_{a,2}}{RT}} \tag{97b}$$

Where $E_{a,1}$ and $E_{a,2}$ are the activation energies.

Most of the works considered just the damage coming from the anode, computing the capacity fade caused by the LLI due to the SEI growth on the particles and its cracks as reported in Eqs. (91)–(96) [35,37–40,118,130].

However, LLI due to the irreversible reactions at the interface between the electrolyte and particle surface is reported to occur in the cathode as well [17,114,115], affecting the capacity degradation of the LIB ultimately. Thus, the LLI occurring both in the anode and cathode needs to be included in the degradation models to achieve an accurate prediction of the LIB capacity decay. However, just few works considered the capacity loss due to cathode fracture [131], although

neglecting the fracture of the anode. Therefore, a complete degradation model combining the performance decay of the anode and cathode is still lacking in the literature. Alternatively, some works estimated the capacity fade due to fracture using empirical models [125,131–133].

6.2. Loss of active material (LAM)

Recently, O'Kane et al. [112] built a model considering capacity loss both from positive and negative electrodes. Besides LLI, the LAM due to particle fracture (according to [134]) was considered. LAM due to particle cracking is modeled estimating the decrease in the accessible volume fraction of active material (ε_a) as a function of the hydrostatic stress, according to Eq. (98) [113,134].

$$\frac{\partial \varepsilon_a}{\partial t} = \frac{\beta_2}{t_N}\left(\frac{\sigma_{h,max} - \sigma_{h,min}}{\sigma_c}\right)^{m_2} \sigma_{h,min} > 0 \tag{98}$$

Where β_2 and m_2 are fitting parameters.

Alternatively, Delacourt and al. [135] developed an empirical model where the accessible volume fraction decreases as a function of the total current density i, as expressed in Eq. (99).

$$\frac{\partial \varepsilon_a}{\partial t} = k_1(T)|i| + k_2(T)\sqrt{|i|} \tag{99}$$

Where $k_1(T)$ and $k_2(T)$ are fitting parameters that depend on temperature.

Narayanrao et al. [136] modeled LAM by decreasing the specific surface area A_a rather than the accessible volume fraction of active material ε_a, according to Eq. (100).

$$\frac{\partial A_a}{\partial t} = -kA_a = -k\frac{3\varepsilon_a}{R} \tag{100}$$

Where k is a fitting constant.

The reduction of the effective active material volume causes a decrease in the available capacity.

Finally, Park et al. [131] modeled the effect of LAM modifying the effective electronic conductivity ($\sigma_{s,crack}$) according to Eq. (101), based on the normalized perimeter change of the cracked particle, which is the index of fracture impact and is experimentally determined.

$$\sigma_{s,crack} = \sigma_{s,0}(1 + k_1 t_c) \tag{101a}$$

$$t_c = tk_2 e^{\frac{(-E_a + k_3 C_{rate})}{RT}} \sum (Normalized\ perimeter\ change)^{k_4} \tag{101b}$$

$$Normalized\ perimeter\ change = \frac{(Cycled\ perimeter - Initial\ perimeter)}{Initial\ perimeter} \tag{101c}$$

Where k_1, k_2, k_3 and k_4 are fitting parameters, $\sigma_{s,0}$ is the initial electronic conductivity, t_c is a degradation factor adopting a power law relationship with time t, E_a is the activation energy, and C_{rate} is the current rate.

6.3. Model results

The main results of physics-based damaging models are reported in Fig. 8. All the results consider only the LLI according to Eqs. (91)–(96) and are quite consistent. Dong et al. [40] modeled capacity fade due to storage and cycling conditions according to the framework explained in this review, but considering a significantly more complex approach. Electron tunneling through the SEI layer is considered rate-limiting in the SEI growth process, making the capacity fade in storage conditions dependent on SOC and temperature. Anyway, SEI growth and the capacity fade in storage conditions follows a logarithmic trend similar to Eq. (89)b. Furthermore, the stress causing crack growth was considered dependent both on the depth of discharge (DOD) and the current rate, making the capacity fade during cycling dependent on DOD and C-rate ultimately. The higher complexity of the model results in a higher number of fitting parameters and complex model calibration. The model was calibrated and validated with empirical laws extrapolated from experimental measurements. It is highlighted that some controversial results come from the model calibration, such as a negative exponential term of Paris' law, which is meaningless [32,34]. The results of their model compared with empirical law based on experimental tests are shown in Fig. 8a.

Deshpande et al. [35] and Li et al. [38] (Fig. 8b) estimated the capacity fade of LFP/graphite cells with constant current (C/2) at different temperatures, finding consistent results.

Verma et al. (Figures 3 and 4 in [37]) and Purewal et al. [118] (Fig. 8c) plotted the different sources of capacity fade as a function of the number of cycles and showed that capacity loss follows a trend $\propto \sqrt{t}$ when the C-rate is low according to Eq. (89)b and Eq. (91). The capacity loss curve becomes steeper when the current rate increases and the amount of damage due to cracks (Eqs. (92) and (94)) becomes significant. The model results follow the experimental curve faithfully for each current rate, confirming that the capacity loss due to crack is significant and meaningful.

Furthermore, Verma et al. [37] compared the results of the coupled model (stress affects diffusion) plotted in Fig. 8c, and the uncoupled model (stress does not affect diffusion). The coupling between stress and diffusion was explained in Section 2 and resumed in Table 1. The results (the reader should refer to Figures 7 and 8 in [37]) show that the uncoupled model overestimates the damaging mechanisms related to fracture because the uncoupled model does not consider the stress mitigation due to diffusion, as explained in previous works [7]. Greater stress leads to a greater increase in crack growth rate according to (93)c, and then greater capacity loss according to the damaging mechanism 2 and 3 (Eqs. (92) and (94)).

Park et al. [131] proposed a degradation model including the effect of the cathode fracture on the capacity loss. The electrochemical behavior of the LIB was modeled using the P2D model. Fracture affects the electrochemical parameters through fitting coefficients which severely affects the reliability of the model. Furthermore, fracture of the anode was not considered.

Some physical parameters involved in the presented models are difficult, if not impossible, to measure. Then, Paris' law parameters (C, or C_0 and $E_{a,1}$, and m), SEI growth rate (k_{SEI}, or $k_{SEI,0}$ and $E_{a,2}$), and the crack density (ρ_c) are fitted on the experimental measures in all the models.

It is interesting to highlight how these models can capture the effect of fracture on the capacity fade. Although some key parameters are fitted, the correspondence between the trend of the model and the experiments is interesting. A possible improvement of these models is to consider a proper geometric factor for Paris' law, the estimation of the crack density based on experimental observations, e.g. using SEM/TEM analysis, and the estimation of Paris' law parameters based on the observation of the crack growth with in-situ SEM/TEM.

6.4. Concluding remarks

The effects of fracture on capacity fade are commonly modeled as loss of lithium inventory because of SEI growth at the negative electrode. The source of capacity fade are three:

- Growth of SEI over the nominal particle surface, which is independent of cracks.
- Formation of a new SEI layer over the surfaces created by the cracks.
- Growth of the SEI layer on the cracks surfaces.

The crack growth, necessary to compute the geometric factor of plates is often used to estimate the SIF. Furthermore, crack density over the active material particles is guessed. These assumptions hinder the reliability of the model.

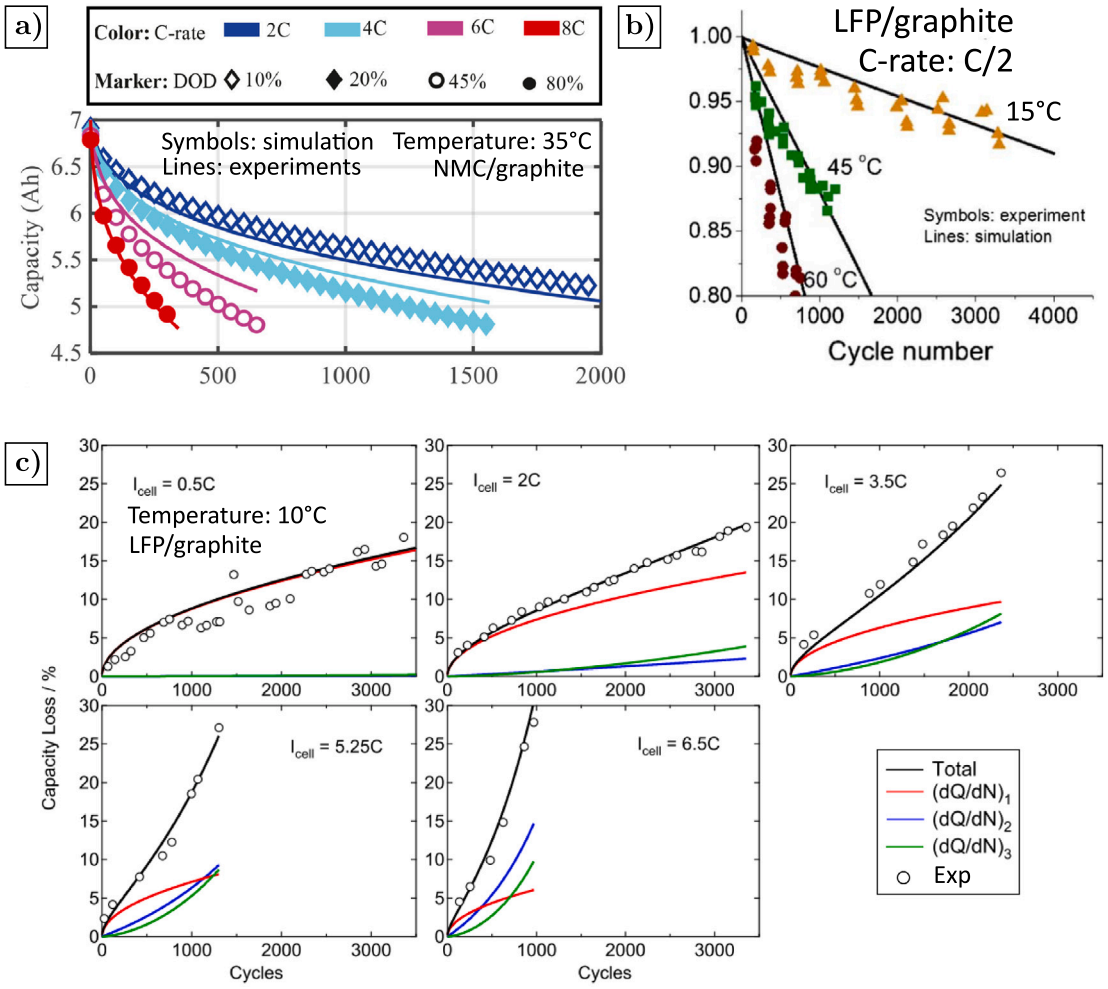

Fig. 8. Capacity fade as a function of the number of cycles in commercial LIBs: comparison between experimental measures and model. (a) Capacity fade in NMC/graphite cells. Reprinted with permission from [40]. (b) Capacity fade in LFP/graphite cells at C/2 and different temperatures. Reprinted with permission from [38]. (c) Capacity fade in LFP/graphite cells, considering the three damaging mechanisms. Reprinted with permission from [118].

However, the trend of capacity fade due to cycling at low C-rate (cracks do not have influence) and at higher C-rate (cracks affect capacity fade) is consistent with experimental studies.

Some models considered the loss of active material caused by cracks as well. The model took into account this mechanism defining a decrease of electrode porosity proportional to the hydrostatic stress.

7. Comments, lacks, and future developments

7.1. Comments

Fracture in LIBs has been extensively studied in the last ten years and a large number of works and models were built. Inevitably, they were defined according to different fracture models, different geometries, and initial assumptions, affecting the consistency among the models.

Fracture mechanics in LIBs has a strong statistical connotation, as the geometry of the particles is irregular and random, and the number and the length of initial defects are unknown and random as well.

Thus, unknown parameters, such as crack density, material properties (K_{cr} and G_{cr}), particle size and shape (thus the geometric factor Y for SIF computation), and TSL law of CZM, affect the reliability of the results.

Most of the results of the models are not consistent with experimental measurements, especially because approximated geometries are considered to simplify calculations and because it is difficult to deal with random properties of the active materials, as explained above.

7.2. Lacks

The main lack is that very few works modeled fatigue fracture due to repeated charge and discharge cycles. Furthermore, most of the works with this aim used an analytical approach based on Paris' law, making strong hypotheses concerning the SIF computation and guessing Paris' parameters, which makes the model unreliable.

7.3. Future developments

Considering the reviewed state of the art, the following research trends are promising and interesting according to the authors:

- A comparison of the fracture behavior of different active materials is necessary, aiming to identify the material with the best performance from the fracture point of view.
- A fatigue fracture model describing the effect of cyclic loads on crack propagation is needed as cracks propagate because of repeated charge/discharge cycles.

- Deep study of damaging mechanisms triggered by fracture is needed to assess the effects of lithium loss inventory caused by degradation reactions and loss of active material on the performance decay of LIBs. Currently, as explained in Section 6, just the loss of lithium inventory due to the SEI growth on graphite was considered. Cathode damage has to be taken into account as well to establish a reliable degradation model.
- A comprehensive correlation between fracture and capacity decay during cycling is needed on the basis of the damaging mechanisms explained in the previous point.
- Accurate experimental measurements have a twofold objective: (a) estimation of the material properties, such as the Paris' law coefficients, or fracture toughness K_{cr} [92,101–104], which are generally assumed; (b) validation of the crack propagation and damaging models. The former can be done by in-situ microscopy techniques. The latter can be done by performing aging tests and statistical analyses.
- Once the influence of fracture on LIBs performance is quantified, it is interesting to investigate how microstructure and operating conditions affect fracture and LIBs performance to get practical design advice.

Declaration of competing interest

The authors declare that they have no known competing financial interests or personal relationships that could have appeared to influence the work reported in this paper.

Data availability

No data was used for the research described in the article.

Appendix A. Additional details of PFM numerical implementation

A.1. Newthon-Raphson method tangent matrices

The expressions of the components of tangent stiffness [**K**] and [**C**] matrices resulting from the Newton–Raphson method are provided in Eqs. (A.1a)–(A.1i) and (A.2a)-(A.2h), respectively.

$$\mathbf{K}^{u}_{ij} = \frac{\partial \mathbf{R}^{u}_{i}}{\partial \mathbf{u}_{j}} = \int_{\Omega} g(d)[\mathbf{B}_{i}]^{T}[\mathbf{C}_{0}][\mathbf{B}_{j}]d\Omega \tag{A.1a}$$

$$\mathbf{K}^{uc}_{ij} = \frac{\partial \mathbf{R}^{u}_{i}}{\partial \mathbf{c}_{j}} = -\int_{\Omega} g(d)[\mathbf{B}^{u}_{i}]^{T}[\mathbf{C}_{0}][\mathbf{I}]8N_{j}\frac{\Omega}{3}d\Omega \tag{A.1b}$$

$$\mathbf{K}^{ud}_{ij} = \frac{\partial \mathbf{R}^{u}_{i}}{\partial \mathbf{d}_{j}} = 0 \tag{A.1c}$$

$$\mathbf{K}^{d}_{ij} = \frac{\partial \mathbf{R}^{d}_{i}}{\partial \mathbf{d}_{j}} = \int_{\Omega}\left[\left(2\mathcal{H} + \frac{G_{cr}}{l_{0}}\right)N_{i}N_{j} + G_{cr}l_{0}[\mathbf{B}_{i}]^{T}[\mathbf{B}_{j}]\right]d\Omega \tag{A.1d}$$

$$\mathbf{K}^{du}_{ij} = \frac{\partial \mathbf{R}^{d}_{i}}{\partial \mathbf{u}_{j}} = 0 \tag{A.1e}$$

$$\mathbf{K}^{dc}_{ij} = \frac{\partial \mathbf{R}^{d}_{i}}{\partial \mathbf{c}_{j}} = 0 \tag{A.1f}$$

$$\mathbf{K}^{c}_{ij} = \frac{\partial \mathbf{R}^{c}_{i}}{\partial \mathbf{c}_{j}} = \int_{\Omega}\left([\mathbf{B}_{i}]D[\mathbf{B}_{i}]N_{j} - [\mathbf{B}_{i}]\frac{D\Omega}{RT}N_{j}[\mathbf{B}_{j}]\hat{\sigma_{h}}\right)d\Omega \tag{A.1g}$$

$$\mathbf{K}^{cu}_{ij} = \frac{\partial \mathbf{R}^{c}_{i}}{\partial \mathbf{u}_{j}} = -\int_{\Omega}[\mathbf{B}_{i}]^{T}\frac{D\Omega\hat{c}}{3RT}[\mathbf{C}_{0}][\mathbf{B}^{u}_{j}]d\Omega \tag{A.1h}$$

$$\mathbf{K}^{cd}_{ij} = \frac{\partial \mathbf{R}^{c}_{i}}{\partial \mathbf{d}_{j}} = 0 \tag{A.1i}$$

$$\boldsymbol{C}^{u}_{ij} = 0 \tag{A.2a}$$

$$\boldsymbol{C}^{uc}_{ij} = 0 \tag{A.2b}$$

$$\boldsymbol{C}^{ud}_{ij} = 0 \tag{A.2c}$$

$$\boldsymbol{C}^{d}_{ij} = 0 \tag{A.2d}$$

$$\boldsymbol{C}^{du}_{ij} = 0 \tag{A.2e}$$

$$\boldsymbol{C}^{dc}_{ij} = 0 \tag{A.2f}$$

$$\boldsymbol{C}^{c}_{ij} = \int_{\Omega} N_{i}N_{j}d\Omega \tag{A.2g}$$

$$\boldsymbol{C}^{cd}_{ij} = 0 \tag{A.2h}$$

Where the subscripts i and j represent the contribution of the i-th and j-th nodes.

Appendix B. Supplementary data

Supplementary material related to this article can be found online at https://doi.org/10.1016/j.jpowsour.2023.232875.

References

[1] C.R. Birkl, M.R. Roberts, E. McTurk, P.G. Bruce, D.A. Howey, Degradation diagnostics for lithium ion cells, J. Power Sources 341 (2017) 373–386.
[2] F. Mocera, A. Somà, D. Clerici, Study of aging mechanisms in lithium-ion batteries for working vehicle applications, in: 2020 Fifteenth International Conference on Ecological Vehicles and Renewable Energies, EVER, IEEE, 2020, pp. 1–8.
[3] J. Newman, K.E. Thomas-Alyea, Electrochemical Systems, John Wiley & Sons, 2004.
[4] X. Zhang, A.M. Sastry, W. Shyy, Intercalation-induced stress and heat generation within single lithium-ion battery cathode particles, J. Electrochem. Soc. 155 (7) (2008) A542.
[5] A. Mukhopadhyay, B.W. Sheldon, Deformation and stress in electrode materials for Li-ion batteries, Prog. Mater. Sci. 63 (2014) 58–116.
[6] J. Christensen, J. Newman, Stress generation and fracture in lithium insertion materials, J. Solid State Electrochem. 10 (5) (2006) 293–319.
[7] D. Clerici, F. Mocera, A. Somà, Analytical solution for coupled diffusion induced stress model for lithium-ion battery, Energies 13 (7) (2020) 1717.
[8] D. Clerici, F. Mocera, A. Somà, Shape influence of active material microstructure on diffusion and contact stress in lithium-ion batteries, Energies 14 (1) (2020) 134.
[9] D. Clerici, F. Mocera, Micro-scale modeling of Lithium-ion battery, in: IOP Conference Series: Materials Science and Engineering, 1038, (1) IOP Publishing, 2021, 012007.
[10] P. Li, Y. Zhao, Y. Shen, S.-H. Bo, Fracture behavior in battery materials, J. Phys.: Energy 2 (2) (2020) 022002.
[11] D. Clerici, F. Mocera, F. Pistorio, Analysis of fracture behaviour in active materials for lithium ion batteries, in: IOP Conference Series: Materials Science and Engineering, 1214, (1) IOP Publishing, 2022, 012018.
[12] D. Clerici, F. Mocera, A. Somà, Experimental characterization of Lithium-ion cell strain using laser sensors, Energies 14 (19) (2021) 6281.
[13] D. Clerici, F. Mocera, A. Somà, Electrochemical–mechanical multi-scale model and validation with thickness change measurements in prismatic lithium-ion batteries, J. Power Sources 542 (2022) 231735.
[14] Y. Zhao, P. Stein, Y. Bai, M. Al-Siraj, Y. Yang, B.-X. Xu, A review on modeling of electro-chemo-mechanics in lithium-ion batteries, J. Power Sources 413 (2019) 259–283.
[15] R. Xu, K. Zhao, Electrochemomechanics of electrodes in Li-ion batteries: A review, J. Electrochem. Energy Convers. Storage 13 (3) (2016).
[16] D. Grazioli, M. Magri, A. Salvadori, Computational modeling of Li-ion batteries, Comput. Mech. 58 (6) (2016) 889–909.
[17] F. Pistorio, D. Clerici, F. Mocera, A. Somà, Review on the experimental characterization of fracture in active material for Lithium-ion batteries, Energies 15 (23) (2022) 9168.
[18] M. Farkhondeh, C. Delacourt, Mathematical modeling of commercial LiFePO4 electrodes based on variable solid-state diffusivity, J. Electrochem. Soc. 159 (2) (2011) A177.
[19] D.R. Baker, M.W. Verbrugge, Intercalate diffusion in multiphase electrode materials and application to lithiated graphite, J. Electrochem. Soc. 159 (8) (2012) A1341.
[20] B. Wu, W. Lu, A consistently coupled multiscale mechanical–electrochemical battery model with particle interaction and its validation, J. Mech. Phys. Solids 125 (2019) 89–111.
[21] G. Bucci, T. Swamy, S. Bishop, B.W. Sheldon, Y.-M. Chiang, W.C. Carter, The effect of stress on battery-electrode capacity, J. Electrochem. Soc. 164 (4) (2017) A645.

[22] E. Bohn, T. Eckl, M. Kamlah, R. McMeeking, A model for lithium diffusion and stress generation in an intercalation storage particle with phase change, J. Electrochem. Soc. 160 (10) (2013) A1638.

[23] M. Torchio, L. Magni, R.B. Gopaluni, R.D. Braatz, D.M. Raimondo, Lionsimba: a matlab framework based on a finite volume model suitable for li-ion battery design, simulation, and control, J. Electrochem. Soc. 163 (7) (2016) A1192.

[24] M. Mastali, M. Farkhondeh, S. Farhad, R.A. Fraser, M. Fowler, Electrochemical modeling of commercial LiFePO4 and graphite electrodes: kinetic and transport properties and their temperature dependence, J. Electrochem. Soc. 163 (13) (2016) A2803.

[25] G.R. Irwin, Analysis of stresses and strains near the end of a crack traversing a plate, 1957.

[26] J.R. Rice, A path independent integral and the approximate analysis of strain concentration by notches and cracks, 1968.

[27] G. Cherepanov, Crack propagation in continuous media: PMM vol. 31, no. 3, 1967, pp. 476–488, J. Appl. Math. Mech. 31 (3) (1967) 503–512, http://dx.doi.org/10.1016/0021-8928(67)90034-2, URL https://www.sciencedirect.com/science/article/pii/0021892867900342.

[28] Y. Gao, M. Zhou, Coupled mechano-diffusional driving forces for fracture in electrode materials, J. Power Sources 230 (2013) 176–193.

[29] H. Haftbaradaran, J. Qu, A path-independent integral for fracture of solids under combined electrochemical and mechanical loadings, J. Mech. Phys. Solids 71 (2014) 1–14.

[30] M. Zhang, J. Qu, J.R. Rice, Path independent integrals in equilibrium electro-chemo-elasticity, J. Mech. Phys. Solids 107 (2017) 525–541.

[31] T.L. Anderson, Fracture Mechanics: Fundamentals and Applications, CRC Press, 2017.

[32] P.C. Paris, A rational analytic theory of fatigue, Trends Engin 13 (1961) 9–14.

[33] P. Paris, F. Erdogan, A critical analysis of crack propagation laws, 1963.

[34] N. Pugno, M. Ciavarella, P. Cornetti, A. Carpinteri, A generalized Paris' law for fatigue crack growth, J. Mech. Phys. Solids 54 (7) (2006) 1333–1349.

[35] R. Deshpande, M. Verbrugge, Y.-T. Cheng, J. Wang, P. Liu, Battery cycle life prediction with coupled chemical degradation and fatigue mechanics, J. Electrochem. Soc. 159 (10) (2012) A1730.

[36] J. Wang, J. Purewal, P. Liu, J. Hicks-Garner, S. Soukazian, E. Sherman, A. Sorenson, L. Vu, H. Tataria, M.W. Verbrugge, Degradation of lithium ion batteries employing graphite negatives and nickel–cobalt–manganese oxide+ spinel manganese oxide positives: Part 1, aging mechanisms and life estimation, J. Power Sources 269 (2014) 937–948.

[37] M. Verma, S. Basu, K.S. Hariharan, S.M. Kolake, T. Song, J. Jeon, A strain-diffusion coupled electrochemical model for lithium-ion battery, J. Electrochem. Soc. 164 (13) (2017) A3426.

[38] J. Li, K. Adewuyi, N. Lotfi, R.G. Landers, J. Park, A single particle model with chemical/mechanical degradation physics for lithium ion battery State of Health (SOH) estimation, Appl. Energy 212 (2018) 1178–1190.

[39] A. Tahmasbi, M. Eikerling, Statistical physics-based model of mechanical degradation in lithium ion batteries, Electrochim. Acta 283 (2018) 75–87.

[40] G. Dong, J. Wei, A physics-based aging model for lithium-ion battery with coupled chemical/mechanical degradation mechanisms, Electrochim. Acta 395 (2021) 139133.

[41] B. Bourdin, G.A. Francfort, J.-J. Marigo, The variational approach to fracture, J. Elasticity 91 (1) (2008) 5–148.

[42] M.J. Borden, C.V. Verhoosel, M.A. Scott, T.J. Hughes, C.M. Landis, A phase-field description of dynamic brittle fracture, Comput. Methods Appl. Mech. Engrg. 217 (2012) 77–95.

[43] C. Miehe, M. Hofacker, F. Welschinger, A phase field model for rate-independent crack propagation: Robust algorithmic implementation based on operator splits, Comput. Methods Appl. Mech. Engrg. 199 (45–48) (2010) 2765–2778.

[44] C. Miehe, H. Dal, L.-M. Schänzel, A. Raina, A phase-field model for chemo-mechanical induced fracture in lithium-ion battery electrode particles, Internat. J. Numer. Methods Engrg. 106 (9) (2016) 683–711.

[45] A. Egger, U. Pillai, K. Agathos, E. Kakouris, E. Chatzi, I.A. Aschroft, S.P. Triantafyllou, Discrete and phase field methods for linear elastic fracture mechanics: a comparative study and state-of-the-art review, Appl. Sci. 9 (12) (2019) 2436.

[46] J.-Y. Wu, V.P. Nguyen, C.T. Nguyen, D. Sutula, S. Sinaie, S.P. Bordas, Phase-field modeling of fracture, Adv. Appl. Mech. 53 (2020) 1–183.

[47] Y. Heider, A review on phase-field modeling of hydraulic fracturing, Eng. Fract. Mech. 253 (2021) 107881.

[48] H. Amor, J.-J. Marigo, C. Maurini, Regularized formulation of the variational brittle fracture with unilateral contact: Numerical experiments, J. Mech. Phys. Solids 57 (8) (2009) 1209–1229.

[49] C. Miehe, F. Welschinger, M. Hofacker, Thermodynamically consistent phase-field models of fracture: Variational principles and multi-field FE implementations, Internat. J. Numer. Methods Engrg. 83 (10) (2010) 1273–1311.

[50] M. Ambati, T. Gerasimov, L. De Lorenzis, A review on phase-field models of brittle fracture and a new fast hybrid formulation, Comput. Mech. 55 (2) (2015) 383–405.

[51] W. Brocks, A. Cornec, I. Scheider, Computational aspects of nonlinear fracture mechanics, Gkss Forschungszentrum Geesthacht Gmbh-Publications-Gkss (30) (2003).

[52] Z. Zou, S. Reid, S. Li, A continuum damage model for delaminations in laminated composites, J. Mech. Phys. Solids 51 (2) (2003) 333–356.

[53] R. Fernandes, J. Chousal, M. De Moura, J. Xavier, Determination of cohesive laws of composite bonded joints under mode II loading, Composites B 52 (2013) 269–274.

[54] I. Scheider, W. Brocks, Simulation of cup–cone fracture using the cohesive model, Eng. Fract. Mech. 70 (14) (2003) 1943–1961.

[55] A. Needleman, V. Tvergaard, An analysis of ductile rupture in notched bars, J. Mech. Phys. Solids 32 (6) (1984) 461–490.

[56] J.T. Wang, Relating cohesive zone model to linear elastic fracture mechanics, Tech. rep., 2010.

[57] V. Tvergaard, Crack growth predictions by cohesive zone model for ductile fracture, J. Mech. Phys. Solids 49 (9) (2001) 2191–2207.

[58] C. Tao, C. Zhang, H. Ji, Y. Wu, J. Qiu, On the energy release rate extraction and mixed mode behavior of fatigue cohesive model, Compos. Struct. 239 (2020) 112038.

[59] W.H. Woodford, Y.-M. Chiang, W.C. Carter, "Electrochemical shock" of intercalation electrodes: a fracture mechanics analysis, J. Electrochem. Soc. 157 (10) (2010) A1052.

[60] R.S. Raghavan, A.M. Kumar, R. Narayanrao, Intercalation induced surface cracking in electrode particles, ZAMM-. Appl. Math. Mech. 95 (8) (2015) 845–858.

[61] A. Singh, S. Pal, Strain gradient enhanced chemo-mechanical modeling of fracture in cathode materials for lithium-ion batteries, Int. J. Solids Struct. 228 (2021) 111098.

[62] B. Chen, J. Zhou, R. Cai, Analytical model for crack propagation in spherical nano electrodes of lithium-ion batteries, Electrochim. Acta 210 (2016) 7–14.

[63] A. Sarkar, P. Shrotriya, A. Chandra, Fracture modeling of lithium-silicon battery based on variable elastic moduli, J. Electrochem. Soc. 164 (11) (2017) E3606.

[64] Y. Murakami, L. Keer, Stress intensity factors handbook, vol. 3, 1993.

[65] S. Al Laham, S.I. Branch, Stress Intensity Factor and Limit Load Handbook, vol. 3, British Energy Generation Limited Gloucester, UK, 1998.

[66] J. Newman, Stress-Intensity Factor Equations for Cracks in Three-Dimensional Finite Bodies Subjected To Tension and Bending Loads, vol. 85793, Langley Research Center, National Aeronautics and Space Administration, 1984.

[67] R.S. Barsoum, On the use of isoparametric finite elements in linear fracture mechanics, Internat. J. Numer. Methods Engrg. 10 (1) (1976) 25–37.

[68] G. Sun, T. Sui, B. Song, H. Zheng, L. Lu, A.M. Korsunsky, On the fragmentation of active material secondary particles in lithium ion battery cathodes induced by charge cycling, Extreme Mech. Lett. 9 (2016) 449–458.

[69] Y. Zhang, C. Zhao, Z. Guo, Simulation of crack behavior of secondary particles in Li-ion battery electrodes during lithiation/de-lithiation cycles, Int. J. Mech. Sci. 155 (2019) 178–186.

[70] Y. Bai, K. Zhao, Y. Liu, P. Stein, B.-X. Xu, A chemo-mechanical grain boundary model and its application to understand the damage of Li-ion battery materials, Scr. Mater. 183 (2020) 45–49.

[71] H. Tian, L.T. Gao, Z.-S. Guo, Microstructural adjusting crack evolution of polycrystalline NCM particle during charge/discharge cycle, J. Electrochem. Soc. 169 (9) (2022) 090513.

[72] H. Tian, L. Gao, P. Huang, Y. Li, Z.-S. Guo, Simulation of intergranular fracture behavior inside randomly aggregated LiNixCoyMn1-x-yO2 polycrystalline particle, Eng. Fract. Mech. 266 (2022) 108381.

[73] R. Grantab, V.B. Shenoy, Location-and orientation-dependent progressive crack propagation in cylindrical graphite electrode particles, J. Electrochem. Soc. 158 (8) (2011) A948.

[74] R. Xu, K. Zhao, Corrosive fracture of electrodes in Li-ion batteries, J. Mech. Phys. Solids 121 (2018) 258–280.

[75] A. Singh, S. Pal, Coupled chemo-mechanical modeling of fracture in polycrystalline cathode for lithium-ion battery, Int. J. Plast. 127 (2020) 102636.

[76] I. Babuška, J.M. Melenk, The partition of unity method, Internat. J. Numer. Methods Engrg. 40 (4) (1997) 727–758.

[77] A.R. Khoei, Extended Finite Element Method: Theory and Applications, John Wiley & Sons, 2014.

[78] K. Rege, H. Lemu, A review of fatigue crack propagation modelling techniques using FEM and XFEM, in: IOP Conference Series: Materials Science and Engineering, 276, (1) IOP Publishing, 2017, 012027.

[79] M. Zhu, J. Park, A.M. Sastry, Fracture analysis of the cathode in Li-ion batteries: A simulation study, J. Electrochem. Soc. 159 (4) (2012) A492.

[80] Y. Zhang, Z. Guo, Numerical computation of central crack growth in an active particle of electrodes influenced by multiple factors, Acta Mech. Sinica 34 (4) (2018) 706–715.

[81] X. Zhu, Y. Chen, H. Chen, W. Luan, The diffusion induced stress and cracking behaviour of primary particle for Li-ion battery electrode, Int. J. Mech. Sci. 178 (2020) 105608.

[82] M. Ahmadi, A hybrid phase field model for fracture induced by lithium diffusion in electrode particles of Li-ion batteries, Comput. Mater. Sci. 184 (2020) 109879.

[83] A. Singh, S. Pal, Chemo-mechanical modeling of inter-and intra-granular fracture in heterogeneous cathode with polycrystalline particles for lithium-ion battery, J. Mech. Phys. Solids 163 (2022) 104839.
[84] R. Xue, X. Li, H. Zhao, Z. Chen, Phase field model coupling with strain gradient plasticity for fracture in lithium-ion battery electrodes, Eng. Fract. Mech. 269 (2022) 108518.
[85] W. Ai, B. Wu, E. Martínez-Pañeda, A coupled phase field formulation for modelling fatigue cracking in lithium-ion battery electrode particles, J. Power Sources 544 (2022) 231805.
[86] M. Klinsmann, D. Rosato, M. Kamlah, R.M. McMeeking, Modeling crack growth during Li insertion in storage particles using a fracture phase field approach, J. Mech. Phys. Solids 92 (2016) 313–344.
[87] A. Mesgarnejad, A. Karma, Phase field modeling of chemomechanical fracture of intercalation electrodes: Role of charging rate and dimensionality, J. Mech. Phys. Solids 132 (2019) 103696.
[88] B. Liu, J. Xu, Cracks of silicon nanoparticles in anodes: Mechanics–electrochemical-coupled modeling framework based on the phase-field method, ACS Appl. Energy Mater. 3 (11) (2020) 10931–10939.
[89] D. T O'Connor, M.J. Welland, W.K. Liu, P.W. Voorhees, Phase transformation and fracture in single LixFePO4 cathode particles: a phase-field approach to Li–ion intercalation and fracture, Modelling Simul. Mater. Sci. Eng. 24 (3) (2016) 035020.
[90] B.-X. Xu, Y. Zhao, P. Stein, Phase field modeling of electrochemically induced fracture in Li-ion battery with large deformation and phase segregation, GAMM-Mitt. 39 (1) (2016) 92–109.
[91] R. Grantab, V.B. Shenoy, Pressure-gradient dependent diffusion and crack propagation in lithiated silicon nanowires, J. Electrochem. Soc. 159 (5) (2012) A584.
[92] R. Xu, H. Sun, L.S. de Vasconcelos, K. Zhao, Mechanical and structural degradation of LiNixMnyCozO2 cathode in Li-ion batteries: an experimental study, J. Electrochem. Soc. 164 (13) (2017) A3333.
[93] J.G. Swallow, W.H. Woodford, F.P. McGrogan, N. Ferralis, Y.-M. Chiang, K.J. Van Vliet, Effect of electrochemical charging on elastoplastic properties and fracture toughness of LiXCoO2, J. Electrochem. Soc. 161 (11) (2014) F3084.
[94] H. Yang, J. Qu, Fracture toughness of LixSi alloys in lithium ion battery, Extreme Mech. Lett. 32 (2019) 100555.
[95] Y. Liu, H. Zheng, X.H. Liu, S. Huang, T. Zhu, J. Wang, A. Kushima, N.S. Hudak, X. Huang, S. Zhang, et al., Lithiation-induced embrittlement of multiwalled carbon nanotubes, Acs Nano 5 (9) (2011) 7245–7253.
[96] Y. Hu, X. Zhao, Z. Suo, Averting cracks caused by insertion reaction in lithium–ion batteries, J. Mater. Res. 25 (6) (2010) 1007–1010.
[97] K. Zhao, M. Pharr, J.J. Vlassak, Z. Suo, Fracture of electrodes in lithium-ion batteries caused by fast charging, J. Appl. Phys. 108 (7) (2010) 073517.
[98] C.-K. ChiuHuang, M.A. Stamps, H.-Y.S. Huang, Mechanics of diffusion-induced fractures in lithium-ion battery materials, MRS Online Proc. Libr. (OPL) 1541 (2013).
[99] C.-K. ChiuHuang, H.-Y.S. Huang, Stress evolution on the phase boundary in LiFePO4 particles, J. Electrochem. Soc. 160 (11) (2013) A2184.
[100] M. Klinsmann, D. Rosato, M. Kamlah, R.M. McMeeking, Modeling crack growth during Li extraction in storage particles using a fracture phase field approach, J. Electrochem. Soc. 163 (2) (2015) A102.
[101] L. De Vasconcelos, N. Sharma, R. Xu, K. Zhao, In-situ nanoindentation measurement of local mechanical behavior of a Li-ion battery cathode in liquid electrolyte, Exp. Mech. 59 (3) (2019) 337–347.
[102] M. Pharr, Z. Suo, J.J. Vlassak, Measurements of the fracture energy of lithiated silicon electrodes of Li-ion batteries, Nano Lett. 13 (11) (2013) 5570–5577.
[103] G. Sun, S. Bhattacharya, A. Alpas, Cyclic strain-induced crack growth in graphite during electrochemical testing in propylene carbonate-based Li-ion battery electrolytes, J. Mater. Sci. 53 (2) (2018) 1297–1309.
[104] Y. Xia, Y. Hirai, T. Tsuchiya, Fracture behavior of single-crystal silicon microstructure coated with stepwise bias-graded aC: H film, Surf. Coat. Technol. 405 (2021) 126559.
[105] Z. Xu, M.M. Rahman, L. Mu, Y. Liu, F. Lin, Chemomechanical behaviors of layered cathode materials in alkali metal ion batteries, J. Mater. Chem. A 6 (44) (2018) 21859–21884.
[106] H.-H. Sun, A. Manthiram, Impact of microcrack generation and surface degradation on a nickel-rich layered Li [Ni0. 9Co0. 05Mn0. 05] O2 cathode for lithium-ion batteries, Chem. Mater. 29 (19) (2017) 8486–8493.
[107] Y.-S. Yu, C. Kim, D.A. Shapiro, M. Farmand, D. Qian, T. Tyliszczak, A.D. Kilcoyne, R. Celestre, S. Marchesini, J. Joseph, et al., Dependence on crystal size of the nanoscale chemical phase distribution and fracture in Li x FePO4, Nano Lett. 15 (7) (2015) 4282–4288.
[108] A.M. Boyce, E. Martínez-Pañeda, A. Wade, Y.S. Zhang, J.J. Bailey, T.M. Heenan, D.J. Brett, P.R. Shearing, Cracking predictions of lithium-ion battery electrodes by X-ray computed tomography and modelling, J. Power Sources 526 (2022) 231119.
[109] X. Cheng, Y. Li, T. Cao, R. Wu, M. Wang, H. Liu, X. Liu, J. Lu, Y. Zhang, Real-time observation of chemomechanical breakdown in a layered nickel-rich oxide cathode realized by in situ scanning electron microscopy, ACS Energy Lett. 6 (5) (2021) 1703–1710.
[110] J.S. Edge, S. O'Kane, R. Prosser, N.D. Kirkaldy, A.N. Patel, A. Hales, A. Ghosh, W. Ai, J. Chen, J. Yang, et al., Lithium ion battery degradation: what you need to know, Phys. Chem. Chem. Phys. 23 (14) (2021) 8200–8221.
[111] M. Kabir, D.E. Demirocak, Degradation mechanisms in Li-ion batteries: a state-of-the-art review, Int. J. Energy Res. 41 (14) (2017) 1963–1986.
[112] S.E. O'Kane, W. Ai, G. Madabattula, D. Alonso-Alvarez, R. Timms, V. Sulzer, J.S. Edge, B. Wu, G.J. Offer, M. Marinescu, Lithium-ion battery degradation: how to model it, Phys. Chem. Chem. Phys. 24 (13) (2022) 7909–7922.
[113] J.M. Reniers, G. Mulder, D.A. Howey, Review and performance comparison of mechanical-chemical degradation models for lithium-ion batteries, J. Electrochem. Soc. 166 (14) (2019) A3189.
[114] A. Tornheim, S. Sharifi-Asl, J.C. Garcia, J. Bareño, H. Iddir, R. Shahbazian-Yassar, Z. Zhang, Effect of electrolyte composition on rock salt surface degradation in NMC cathodes during high-voltage potentiostatic holds, Nano Energy 55 (2019) 216–225.
[115] Z. Wang, Z. Wang, D. Xue, J. Zhao, X. Zhang, L. Geng, Y. Li, C. Du, J. Yao, X. Liu, et al., Reviving the rock-salt phases in Ni-rich layered cathodes by mechano-electrochemistry in all-solid-state batteries, Nano Energy 105 (2023) 108016.
[116] M. Safari, C. Delacourt, Simulation-based analysis of aging phenomena in a commercial graphite/LiFePO4 cell, J. Electrochem. Soc. 158 (12) (2011) A1436.
[117] G. Ning, B. Haran, B.N. Popov, Capacity fade study of lithium-ion batteries cycled at high discharge rates, J. Power Sources 117 (1–2) (2003) 160–169.
[118] J. Purewal, J. Wang, J. Graetz, S. Soukiazian, H. Tataria, M.W. Verbrugge, Degradation of lithium ion batteries employing graphite negatives and nickel–cobalt–manganese oxide+ spinel manganese oxide positives: Part 2, chemical–mechanical degradation model, J. Power Sources 272 (2014) 1154–1161.
[119] A. Krupp, R. Beckmann, T. Diekmann, E. Ferg, F. Schuldt, C. Agert, Calendar aging model for lithium-ion batteries considering the influence of cell characterization, J. Energy Storage 45 (2022) 103506.
[120] D. Werner, S. Paarmann, T. Wetzel, Calendar aging of Li-ion cells—Experimental investigation and empirical correlation, Batteries 7 (2) (2021) 28.
[121] S.J. An, J. Li, C. Daniel, D. Mohanty, S. Nagpure, D.L. Wood III, The state of understanding of the lithium-ion-battery graphite solid electrolyte interphase (SEI) and its relationship to formation cycling, Carbon 105 (2016) 52–76.
[122] G. Ning, B.N. Popov, Cycle life modeling of lithium-ion batteries, J. Electrochem. Soc. 151 (10) (2004) A1584.
[123] P. Ramadass, B. Haran, P.M. Gomadam, R. White, B.N. Popov, Development of first principles capacity fade model for Li-ion cells, J. Electrochem. Soc. 151 (2) (2004) A196.
[124] M.B. Pinson, M.Z. Bazant, Theory of SEI formation in rechargeable batteries: capacity fade, accelerated aging and lifetime prediction, J. Electrochem. Soc. 160 (2) (2012) A243.
[125] H. Ekström, G. Lindbergh, A model for predicting capacity fade due to SEI formation in a commercial graphite/LiFePO4 cell, J. Electrochem. Soc. 162 (6) (2015) A1003.
[126] N. Kamyab, J.W. Weidner, R.E. White, Mixed mode growth model for the solid electrolyte interface (SEI), J. Electrochem. Soc. 166 (2) (2019) A334.
[127] S.K. Rahimian, M.M. Forouzan, S. Han, Y. Tang, A generalized physics-based calendar life model for Li-ion cells, Electrochim. Acta 348 (2020) 136343.
[128] M. Safari, M. Morcrette, A. Teyssot, C. Delacourt, Multimodal physics-based aging model for life prediction of Li-ion batteries, J. Electrochem. Soc. 156 (3) (2008) A145.
[129] E. Prada, D. Di Domenico, Y. Creff, J. Bernard, V. Sauvant-Moynot, F. Huet, A simplified electrochemical and thermal aging model of LiFePO4-graphite Li-ion batteries: power and capacity fade simulations, J. Electrochem. Soc. 160 (4) (2013) A616.
[130] G. Hwang, N. Sitapure, J. Moon, H. Lee, S. Hwang, J.S.-I. Kwon, Model predictive control of lithium-ion batteries: Development of optimal charging profile for reduced intracycle capacity fade using an enhanced single particle model (SPM) with first-principled chemical/mechanical degradation mechanisms, Chem. Eng. J. 435 (2022) 134768.
[131] S.H. Park, H. Lee, J. Park, Y. Roh, S. Byun, J. Lim, S. Jung, N. Kim, K.T. Lee, Y.M. Lee, A microcrack propagation-based life prediction model for lithium-ion batteries with Ni-rich cathode materials, J. Energy Storage 58 (2023) 106420.
[132] P. Barai, K. Smith, C.-F. Chen, G.-H. Kim, P.P. Mukherjee, Reduced order modeling of mechanical degradation induced performance decay in lithium-ion battery porous electrodes, J. Electrochem. Soc. 162 (9) (2015) A1751.
[133] F.M. Kindermann, J. Keil, A. Frank, A. Jossen, A SEI modeling approach distinguishing between capacity and power fade, J. Electrochem. Soc. 164 (12) (2017) E287.
[134] I. Laresgoiti, S. Käbitz, M. Ecker, D.U. Sauer, Modeling mechanical degradation in lithium ion batteries during cycling: Solid electrolyte interphase fracture, J. Power Sources 300 (2015) 112–122.
[135] C. Delacourt, M. Safari, Life simulation of a graphite/LiFePO4 cell under cycling and storage, J. Electrochem. Soc. 159 (8) (2012) A1283.
[136] R. Narayanrao, M.M. Joglekar, S. Inguva, A phenomenological degradation model for cyclic aging of lithium ion cell materials, J. Electrochem. Soc. 160 (1) (2012) A125.